A Comprehensive Study of the Young Cluster IRAS 05100+3723: Properties, Surrounding Interstellar Matter, and Associated Star Formation

R. K. Yadav, M. R. Samal, E. Semenko, A. Zavagno, N. Panwar, S. Vaddi, P. Prajapati, D. K. Ojha, A. K. Pandey, M. Ridsdill-Smith, et al.

▶ **To cite this version:**

R. K. Yadav, M. R. Samal, E. Semenko, A. Zavagno, N. Panwar, et al.. A Comprehensive Study of the Young Cluster IRAS 05100+3723: Properties, Surrounding Interstellar Matter, and Associated Star Formation. The Astrophysical Journal, 2022, 926, 10.3847/1538-4357/ac3a78 . insu-03667470

HAL Id: insu-03667470

https://insu.hal.science/insu-03667470

Submitted on 13 May 2022

HAL is a multi-disciplinary open access archive for the deposit and dissemination of scientific research documents, whether they are published or not. The documents may come from teaching and research institutions in France or abroad, or from public or private research centers.

L'archive ouverte pluridisciplinaire **HAL**, est destinée au dépôt et à la diffusion de documents scientifiques de niveau recherche, publiés ou non, émanant des établissements d'enseignement et de recherche français ou étrangers, des laboratoires publics ou privés.

Distributed under a Creative Commons Attribution 4.0 International License

The Astrophysical Journal, 926:16 (20pp), 2022 February 10 https://doi.org/10.3847/1538-4357/ac3a78
© 2022. The Author(s). Published by the American Astronomical Society.
OPEN ACCESS

A Comprehensive Study of the Young Cluster IRAS 05100+3723: Properties, Surrounding Interstellar Matter, and Associated Star Formation

R. K. Yadav[1], M. R. Samal[2], E. Semenko[1], A. Zavagno[3,4], S. Vaddi[5], P. Prajapati[2], D. K. Ojha[6], A. K. Pandey[7,11], M. Ridsdill-Smith[1], J. Jose[8], S. Patra[8], S. Dutta[9], P. Irawati[1], S. Sharma[7], D. K. Sahu[10], and N. Panwar[7]
[1] National Astronomical Research Institute of Thailand (NARIT), Sirindhorn AstroPark, 260 Moo 4, T. Donkaew, A. Maerim, Chiangmai 50180, Thailand
ram_kesh@narit.or.th
[2] Physical Research Laboratory, Navrangpura, Ahmedabad, Gujarat 380009, India
[3] Aix-Marseille Universite, CNRS, CNES, LAM, Marseille, France
[4] Institut Universitaire de France, Paris, France
[5] National Centre for Radio Astrophysics (TIFR), Post Bag 3, Ganeshkhind, Pune 411007, India
[6] Department of Astronomy and Astrophysics, Tata Institute of Fundamental Research, Homi Bhabha Road, Mumbai 400005, India
[7] Aryabhatta Research Institute of Observational Sciences (ARIES), Nainital 263129, India
[8] Indian Institute of Science Education and Research (IISER) Tirupati, Rami Reddy Nagar, Karakambadi Road, Mangalam (P.O.), Tirupati 517 507, India
[9] Institute of Astronomy and Astrophysics, Academia Sinica, Taipei 10617, Taiwan
[10] Indian Institute of Astrophysics, II Block, Koramangala, Bengaluru 560 034, Karnataka, India
Received 2021 June 16; revised 2021 November 14; accepted 2021 November 15; published 2022 February 8

Abstract

We present a comprehensive multiwavelength investigation of a likely massive young cluster "IRAS 05100+3723" and its environment with the aim to understand its formation history and feedback effects. We find that IRAS 05100 +3723 is a distant (∼3.2 kpc), moderate-mass (∼500 $M_{\odot}$), young (∼3 Myr) cluster with its most massive star being an O8.5V type. From spectral modeling, we estimate the effective temperature and log g of the star to be ∼33,000 K and ∼3.8, respectively. Our radio continuum observations reveal that the star has ionized its environment, forming a H II region of size ∼2.7 pc, temperature ∼5700 K, and electron density ∼165 cm^{-3}. However, our large-scale dust maps reveal that it has heated the dust up to several parsecs (∼10 pc) in the range 17−28 K and the morphology of warm dust emission resembles a bipolar H II region. From dust and ^{13}CO gas analyses, we find evidence that the formation of the H II region has occurred at the very end of a long filamentary cloud around 3 Myr ago, likely due to edge collapse of the filament. We show that the H II region is currently compressing a clump of mass ∼2700 $M_{\odot}$ at its western outskirts, at the junction of the H II region and filament. We observe several 70 μm point sources of intermediate mass and class 0 nature within the clump. We attribute these sources as the second-generation stars of the complex. We propose that the star formation in the clump is either induced or being facilitated by the compression of the expanding H II region onto the inflowing filamentary material.

Unified Astronomy Thesaurus concepts: Star formation (1569); Protostars (1302); Pre-main sequence stars (1290); Star clusters (1567); Interstellar filaments (842); H II regions (694); Interstellar extinction (841); Interstellar dust (836); Molecular clouds (1072)

1. Introduction

It is believed that most, if not all, stars form in embedded clusters (Lada & Lada 2003). In general, parsec-scale young clusters (age > 2 Myr) have smooth, centrally condensed and nearly spherical structures (Ascenso et al. 2007; Harayama et al. 2008), while molecular clouds, in general, have an irregular and much extended (up to tens of parsecs) structure (André et al. 2008; Molinari et al. 2010). In this context, a key question is "How do centrally condensed clusters form from such molecular clouds?" Although there are various proposed mechanisms of cluster formation such as the monolithic collapse of molecular clouds, hierarchical collapse and merger of gas and star(s), and global nonisotropic collapse (Longmore et al. 2014; Banerjee & Kroupa 2015; Motte et al. 2018; Vázquez-Semadeni et al. 2019), it is yet unclear which process plays a dominant role under which circumstances. Moreover, it is not known if other dynamical processes such as two-body relaxation and mass segregation are also responsible for shaping the structure of the newly born clusters (Banerjee & Kroupa 2017; Sills et al. 2018). These questions can be addressed by studying young clusters while they are still associated with gas and dust. Another key question related to cluster formation, particularly associated with the formation of massive to intermediate-mass clusters, is whether such clusters play a constructive or destructive role in the future star formation processes of the host cloud. This is because massive members of such clusters, on one hand, can switch off the star formation by blowing off the gas and dust from their immediate vicinity, and, on the other hand, can compress the cold parental gas to promote the star formation (Elmegreen & Lada 1977; Deharveng et al. 2010) in the cloud. And the latter can prolong the star formation activity of a molecular cloud up to several million years (e.g., Preibisch & Mamajek 2008).

In the past, studying the early evolution of young clusters had been an observational challenge as they are buried inside molecular clouds. Recent sensitive surveys over the last decade, however, have provided a wealth of data in the optical to millimeter domain (e.g., Jackson et al. 2006; Lawrence et al. 2007; Minniti et al. 2010; Molinari et al. 2010; Chambers et al. 2016; Gaia Collaboration et al. 2016). These surveys allow us

[11] Deceased.

Original content from this work may be used under the terms of the Creative Commons Attribution 4.0 licence. Any further distribution of this work must maintain attribution to the author(s) and the title of the work, journal citation and DOI.

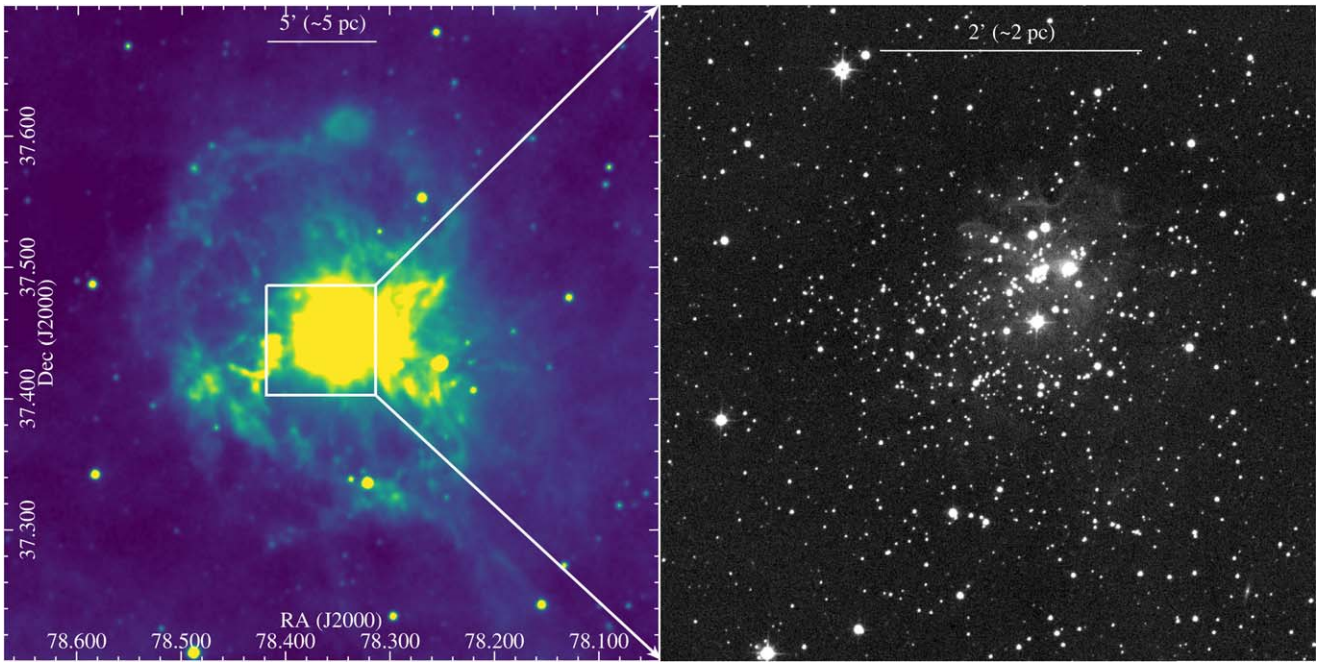

Figure 1. The left panel displays the WISE 12 μm image dust distribution around the cluster having an area of 30×30 arcmin^2, while the right panel displays the UKDISS H-band image of the central 5×5 arcmin^2 area.

to better understand the properties of the young clusters and characterize the physical conditions of the surrounding interstellar medium (ISM). For example, by using parallax and proper-motion (PM) measurements obtained from the Gaia (Gaia Collaboration et al. 2016, 2018) survey data, distances to the star clusters can be precisely estimated (Bailer-Jones et al. 2018) and membership of the bright stars can be well constrained. Similarly, using deep infrared data sets from surveys such as the Galactic Plane Survey from the UKIRT Infrared Deep Sky Survey (UKIDSS-GPS; Lucas et al. 2008), the Spitzer Galactic Legacy Infrared Mid-Plane Survey Extraordinaire (GLIMPSE; Whitney & GLIMPSE360 Team 2009), and the Wide-field Infrared Survey Explorer (WISE; Wright et al. 2010), pre-main-sequence (PMS) members of the young clusters can be identified (e.g., Gutermuth et al. 2009; Das et al. 2021). Moreover, for moderately extincted nearby clusters, age determination is possible by constructing color–magnitude diagrams (CMDs) using data from optical surveys such as Gaia (Gaia Collaboration et al. 2018), the Panoramic Survey Telescope and Rapid Response System (Pan-STARRS1; Chambers et al. 2016) and the Sloan Digital Sky Survey (SDSS; Alam et al. 2015). In addition to that, using wide area maps provided by surveys such as the Herschel Infrared Galactic Plane Survey (Hi-GAL Pilbratt et al. 2010; Molinari et al. 2010) and the Five College Radio Astronomical Observatory (FCRAO; Jackson et al. 2006), connections between the large-scale environment and the cluster-forming clumps can be made.

In the present work, we characterize the young cluster IRAS 05100+3723 (Bica et al. 2003) associated with the H II region Sharpless 228 (hereafter S228, Sharpless 1959), also known as LBN 784 and RAFGL 5137 ($\alpha_{2000} = 78.^\circ356250$, $\delta_{2000} = +37.^\circ450278$). The H II region is believed to be powered by a massive star ALS 19710 of spectral type between O8V and B0V, whose reddening ($E(B-V)$), lies in the range 1.2−1.3 mag (Chini & Wink 1984; Hunter & Massey 1990). We study the physical conditions of dust and gas around the cluster by taking advantage of the key strengths of the aforementioned multi-wavelength surveys. Figure 1 shows the WISE 12 μm image around the cluster over a 30×30 arcmin^2 area as well as the central 5×5 arcmin^2 area in the near-infrared (NIR) H band from the UKIDSS-GPS (Lucas et al. 2008) wherein the cluster is clearly visible. There are several shallow optical and infrared studies of the cluster suggesting that the cluster is located at a distance of between 2.2 and 6.8 kpc and its age lies somewhere between 1 and 25 Myr (Lahulla 1985; Hunter & Massey 1990; Kharchenko et al. 2013; Yu et al. 2018). To date, the most detailed work on the cluster has been carried out by Borissova et al. (2003) using NIR observations. Their results suggest that the age of the cluster is ∼3 Myr and its total stellar mass is ∼1800 $M_\odot$. This makes the cluster one of the potential young massive clusters in our Galaxy, such as the Orion Nebula Cluster (ONC, mass ∼2000 $M_\odot$ and age ∼3 Myr; see Hillenbrand 1997; Da Rio et al. 2010), albeit at a farther distance. Borissova et al. (2003) estimated the cluster radius to be 1.′5 while Yu et al. (2018) reported the cluster radius to be 2.′5.

Intermediate-mass to massive young clusters are rare in our Galaxy. For example, Lada & Lada (2003), in their study of young (<3 Myr) embedded clusters within 2 kpc of the solar neighborhood, found that the only cluster that has a stellar mass of >1000 $M_\odot$ is the ONC. Thus, a cluster like IRAS 05100 +3723 serves as a potential candidate for understanding the formation and early evolution of intermediate-mass to massive clusters. Despite the fact that IRAS 05100+3723 is a potentially young massive cluster, its detailed stellar content, physical properties, and surrounding ISM are scarcely explored. In this work, we examine the stellar, gaseous, and dust components of this likely massive cluster and its environment, with the aim to understand its formation history and feedback effects on the star formation processes of the host cloud.

We organize this paper as follows. In Section 2 we present the observations, archival data sets and data reduction procedures. Section 3 discusses the stellar content and

Table 1
Log of the MRES Observations

ID	α_{2000} (°)	δ_{2000} (°)	Date of Observation	V (mag)	Exposure Time (s)
1	078.356250	+37.458222	2019-03-18	12.6	2700
2	078.356667	+37.458167	2019-03-18	13.2	3000
3	078.353333	+37.453250	2019-03-18	13.1	3000

properties of the cluster, and the physical conditions and kinematics of the large-scale environment. Section 4 discusses the dynamical status of the cluster, its formation history, and the effect of stellar feedback on the star formation scenario of the complex, followed by a summary in Section 5.

2. Observations and Data Sets

2.1. Optical Spectroscopic Observations

We obtained medium-resolution spectra for three bright stars in the S228 complex using the Medium Resolution Spectrograph (MRES) mounted on the 2.4 m Thai National Telescope (TNT). The MRES is a fiber-fed echelle spectrograph designed to work in spectral range of 3900 −8800 Å with a spectral resolution of R ∼16,000−19,000. This instrument is equipped with a 2048 × 512 pixels Andor CCD camera with a pixel size of 13.5 μm.

The data were acquired on the night of 2019 March 18 with a lunar illumination of ∼80% during partially cloudy weather conditions. The log of the observations is given in Table 1. In addition to the science spectra, we obtained standard calibration frames such as bias, flat, and Th-Ar lamp. The data reduction was carried out using the ECHELLE standard package of IRAF. The spectra were extracted using optimal extraction methods. The wavelength calibration of the spectra was done using the Th-Ar lamp source. The wavelength calibrated, normalized spectra of the three stars are shown in Figure 2. We discuss the spectral classification of these stars in Section 3.1.1. It should be noted that only a part of the spectra, in the range 4400 −6800 Å, is being used in this work. The spectra in the range 3900−4400 Å are dominated by noise due to poor sensitivity in this range, and spectra beyond 6800 Å are dominated by multiple telluric lines/bands and hence not used in our analysis.

2.2. Radio Continuum Observations

Radio continuum observations of the S228 region were obtained at 610 and 1280 MHz using the GMRT array (PI: M. R. Samal, ID: 13MRS01) with the aim to trace the ionized gas content of the cluster. The GMRT array consists of 30 antennas arranged in an approximate Y-shaped configuration, with each antenna having a diameter of 45 m. Details about the GMRT can be found in Swarup et al. (1991).

The Very Large Array (VLA) phase and flux calibrators "0555+398" and "3C48," respectively, were used for these observations. We carried out the data reduction using the AIPS software and followed the procedure described in Mallick et al. (2013). Briefly, we used various AIPS tasks for flagging the bad data and calibrating the data with standard phase and flux calibrators. Thereafter, we ran the AIPS task "IMAGR" to make maps after splitting the source data from the whole observations. We applied a few iterations of (phase) self-calibration to remove ionospheric phase distortion effects. The resultant maps are discussed in Section 3.2.1.

2.3. Ancillary Archival Data Sets

For the present work, we have also used the following archival data sets covering various wavelengths:

(i) Gaia Early Data Release 3 (Gaia EDR3 Gaia Collaboration et al. 2021) from the European Space Agency Gaia mission (Gaia Collaboration et al. 2016). We used the kinematic information of Gaia data to estimate the distance to the cluster. The effective angular resolution of the survey is ∼0.″4.

(ii) The Spitzer IRAC warm mission data at 3.6 and 4.5 μm (PI: Barbara Whitney, Program ID: 61070) from the Spitzer Heritage Archive (SHA). We acquired the corrected basic calibrated data (cbcd), uncertainty (cbunc), and imask (bimsk) files. In order to create the final mosaic images with a pixel scale of 1.″2 pixel^{-1}, and to obtain the aperture photometry of the point sources, we followed the steps mentioned in Yadav et al. (2016) and used sources with uncertainty <0.2 mag for our analysis.

(iii) The NIR (J, H, and K) photometric data from UKIDSS-GPS (Lucas et al. 2008), with uncertainty <0.2 mag in all three bands. The spatial resolution of the UKIDSS-GPS data is in the range 0.″8–1″.

(iv) The INT/WFC Photometric Hα Survey of the Northern Galactic Plane (IPHAS) Data Release 2 (Barentsen et al. 2014) photometric data with uncertainty <0.2 mag in Sloan r and i broadband and Hα narrowband filters. The spatial resolution of the IPHAS data is in the range 0.″8–1″.

(v) The Pan-STARRS1 (hereafter; PS1 Chambers et al. 2016) survey photometric data with uncertainty <0.2 mag in $i_{\rm P1}$ and $z_{\rm P1}$ bands were used to estimate the age of the cluster. The spatial resolution of the PS1 data is in the range 0.″8−1″.

(vi) The far-infrared images from the Herschel Infrared Galactic Plane Survey (Hi-GAL; Molinari et al. 2010) images at 70, 160, 250, 350, and 500 μm were used. The spatial resolution of the Hi-Gal observation at 70, 160, 250, 350, and 500 μm bands is 8.″5, 13.″5, 18.″2, 24.″9, and 36.″3, respectively.

(vii) The radio continuum image at 8700 from the National Radio Astronomy Observatory (NRAO) data archive (Project ID: AR390). The beam size of the image is ∼10″×8″ and its rms noise is ∼0.1 μJy beam^{-1}.

(viii) The radio continuum image at 150 MHz from the TIFR GMRT Sky Survey (TGSS; Intema et al. 2017). The typical resolution of the TGSS images is ∼25″×25″ with a median noise of ∼3.5 mJy beam^{-1}.

2.3.1. Completeness of Photometric Data

In this work, we used UKDISS, Spitzer IRAC, and IPHAS data sets to access the young stellar content of the cluster. We obtained the completeness limits of these bands using the histogram turnover method. Although this method is not a formal tool to measure the completeness, it serves as a proxy to give the typical value of the completeness limit across the field (e.g., Samal et al. 2015; Damian et al. 2021). In this approach, the magnitude at which the histogram deviates from the linear distribution is, in general, considered to be 90% complete. Figure 3 shows histograms of sources detected in various bands over a radius of ∼2.′5 (see Section 1). The above approach suggests, in general, our photometry is ∼90% complete down

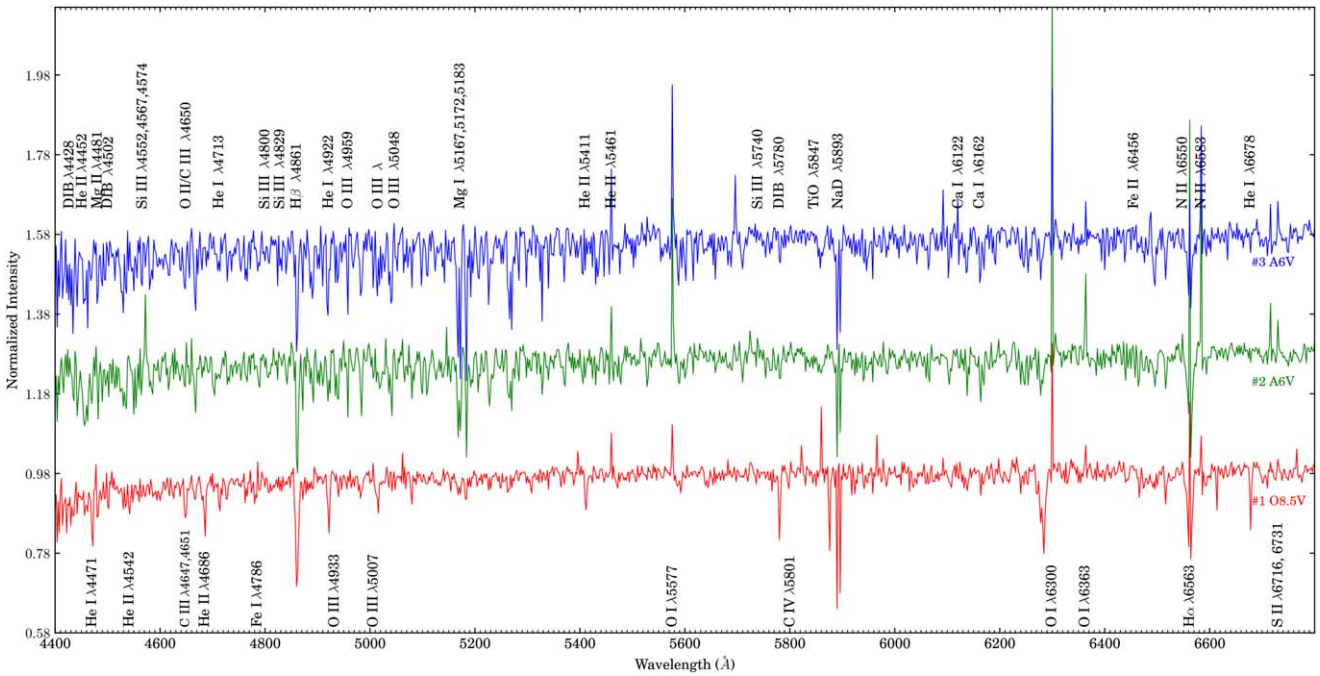

Figure 2. Continuum normalized and scaled spectra of three bright stars #1, #2, and #3 observed with MRES mounted on TNT. Important stellar lines are marked.

to $J = 17.8$ mag, $H = 16.8$ mag, $K = 16.2$ mag, and $[4.5] = 15.5$ mag; these are marked by vertical lines in Figure 3. Similarly, we also estimated the completeness limits of IPHAS r, Hα, and i; and PS1 $i_{\rm P1}$ and $z_{\rm P1}$ bands as 20.3 mag, 19.8 mag, and 19.0 mag; and 20.4, and 19.7 mag, respectively.

3. Analysis and Results

3.1. Stellar Content and Properties of the Cluster

In this section, we access massive and low-mass stellar content of the cluster and derive cluster properties using various photometric catalogs.

3.1.1. Spectral Classification and Modeling of the Bright Sources

The cluster IRAS 05100+3723 is associated with an H II region, implying that its massive members must be responsible for the ionization of the region. To identify the ionizing source(s) of the H II region, we selected three bright sources located within the region of strong Hα emission. Following Comerón & Pasquali (2005), we use the infrared reddening-free pseudo color index, $Q = (J - H) - 1.70 \times (H - K)$ and select sources with $Q < 0.1$ as probable OB stars of the region. These sources are marked in Figure 4 as #1, #2, and #3. However, selected sources may be contaminated by objects such as AGB stars, carbon stars, and A-type giants (Comerón & Pasquali 2005). We thus performed optical spectroscopic analyses of these three bright sources.

As mentioned in Section 2.1, observations were carried out under cloudy weather conditions during the waxing Moon with 80% illumination. This caused the stellar spectra to be heavily contaminated with solar lines. The contamination becomes more obvious upon close examination of the spectra (Figures 2 and 5). The variable contamination of stellar spectra restricts our ability to find accurate physical parameters of the stars, but the spectra still contain enough markers of the effective temperature.

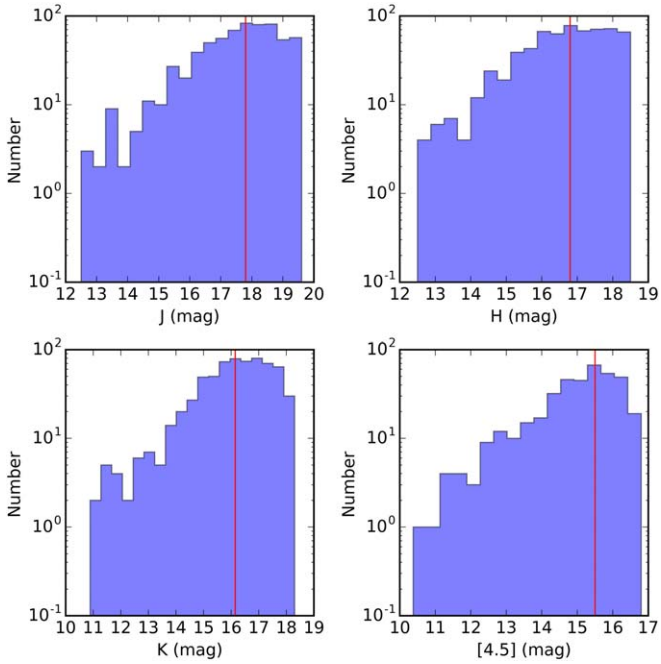

Figure 3. Histograms of the sources detected in J, H, K, and [4.5] μm photometric bands. The vertical red lines indicate the 90% completeness limit. See the text for details.

The abundance of neutral and/or ionized helium lines in absorption is indicative of O or early B type main-sequence stars. These lines may be in emission in the case of giants/supergiants. The strength of He II 4686 gets weaker for late O type stars, and this line is last seen in B0.5 stars (Walborn & Fitzpatrick 1990). We could find such lines only in the spectrum of star #1. To further constrain this, we compare our data with synthetic spectra computed for different combinations of effective temperature, surface gravity, and projected rotational velocity. Theoretical spectra were synthesized with

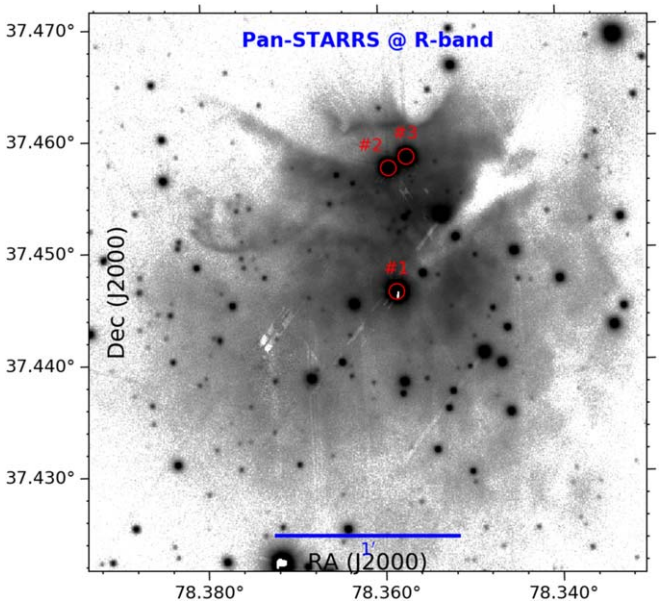

Figure 4. Pan-STARRS r-band image of the cluster along with the sources for which spectroscopic observations have been conducted. The ID and the coordinates of the sources are given in Table 1.

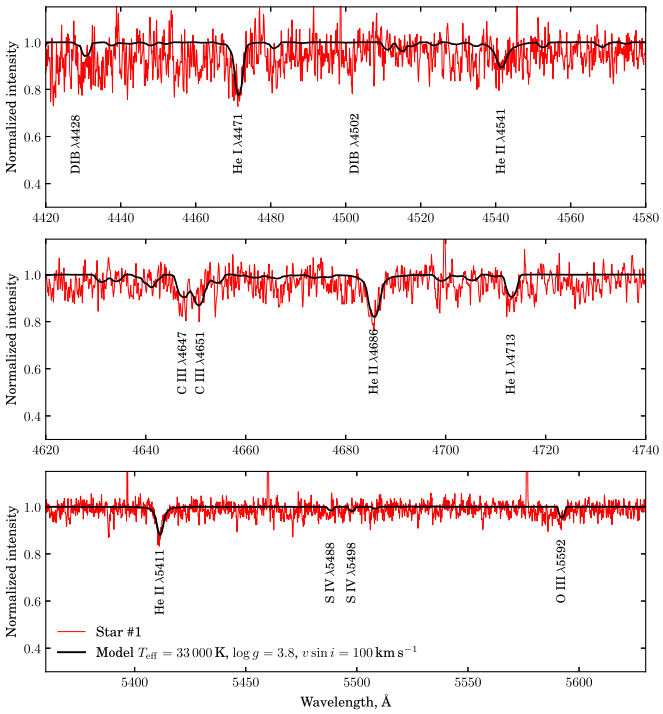

Figure 5. Part of the MRES spectrum (red) for the source #1 fitted with a synthetic profile (black). The synthetic spectrum was computed using the parameters specified in the text.

SYNPLOT, an IDL-based wrapper of the SYNSPEC package for spectral synthesis (Hubeny & Lanz 2011). We use the "OSTAR2002" grid of precomputed models of Lanz & Hubeny (2003).

In the observed spectrum, we identified multiple neutral and ionized helium, carbon, and oxygen lines (Figure 5). Among them, two helium lines, He I λ4471 and He II λ4541, are good indicators of effective temperature. The intensity ratio of these lines equals to 1 for the spectral class O7 (Walborn & Fitzpatrick 1990) and it varies between >1 and <1 for the spectral range O5−O9. This intensity ratio for star #1 is estimated to be <1. By fitting the synthetic spectrum, we derive the effective temperature $T_{\rm eff} = 33{,}000 \pm 1000$ K and surface gravity $\log g = 3.8 \pm 0.5$ (Figure 5), which allowed us to classify this object as an O8.5V $\pm$ 0.5 star. The synthetic spectrum was computed for $T_{\rm eff} = 33{,}000 \pm 1000$ K, $\log g = 3.8 \pm 0.5$, and $v \sin i = 100 \pm 50$ km s^{-1} for the whole wavelength range, which agrees well with the observed lines in other spectral regions and thereby verifies our estimates.

The spectral types of the two fainter stars are less certain. Their spectra do not contain any measurable lines of helium, which are typical of OB stars. Instead, from the comparison with the solar spectrum we identified neutral iron, chromium, and titanium (see Figure 2) lines. Detailed modeling of these spectra was carried out using the NEMO grids of stellar atmospheres computed with a modified version of the ATLAS9 code (Heiter et al. 2002). The modeling results show that star #2 is hotter than the Sun and has an effective temperature of 7000 ± 1000 K, whereas the star #3 looks comparatively cooler with a probable effective temperature of 6400 K. The existing data do not allow us to determine the surface gravity (and thus the evolutionary status) of these stars with a higher accuracy. Our spectral analysis suggests that stars #2 and #3 are late A to F type stars. Indeed, the Gaia data confirmed that stars #2 and #3 are foreground objects, as discussed in Section 3.1.3.

3.1.2. Physical Extent

We derived the physical extent of the cluster by generating the stellar surface density map (SSDM) using UKDISS point sources. In order to generate the SSDM map, we used the nearest neighbors algorithm as described in Gutermuth et al. (2005). Succinctly, at each sample position $[i, j]$ in a uniform grid, we measured $r_N(i, j)$, the projected radial distance to the $N^{\rm th}$ nearest star. N is allowed to vary to the desired smallest scale structures of interest. We generated the map using $N = 20$, which, after a series of tests, was found to be a good compromise between the resolution and signal-to-noise ratio of the map. The resultant map is shown in Figure 6 (upper panel) along with stellar surface density contours. We then considered the peak (at $\alpha_{2000} = 78\overset{\circ}{.}366083$ $\delta_{2000} = +37\overset{\circ}{.}444889$) of the SSDM map as the cluster center.

We also constructed a radial density profile (RDP) of the cluster. The RDP is generated by plotting the annular stellar density against the corresponding radius (for details, see Panwar et al. 2019). In order to parameterize the RDP, the observed RDP is fitted with the empirical King profile (King 1962), which is of the form:

$$\rho(r) \propto b_0 + \frac{\rho_0}{\left(1 + \left(\frac{r}{r_c}\right)^2\right)} \quad (1)$$

where b_0, ρ_0, and r_c are the background stellar density, peak density, and core radius, respectively. The fitted King profile, shown in the lower panel of Figure 6, yields a central density of $\rho_0 = 116$ stars arcmin^{-2}, a core radius of $r_c = 0\overset{'}{.}8$, and a background density $b_0 = 13$ stars arcmin^{-2}. From Figure 6, we note that the model profile merges with the background density at $2\overset{'}{.}5$ and is almost constant beyond the radius of $\sim 3\overset{'}{.}0$. We thus considered the radius of the cluster to be $2\overset{'}{.}5$. The estimated radius is in agreement with the cluster size of $5\overset{'}{.}2$ (or

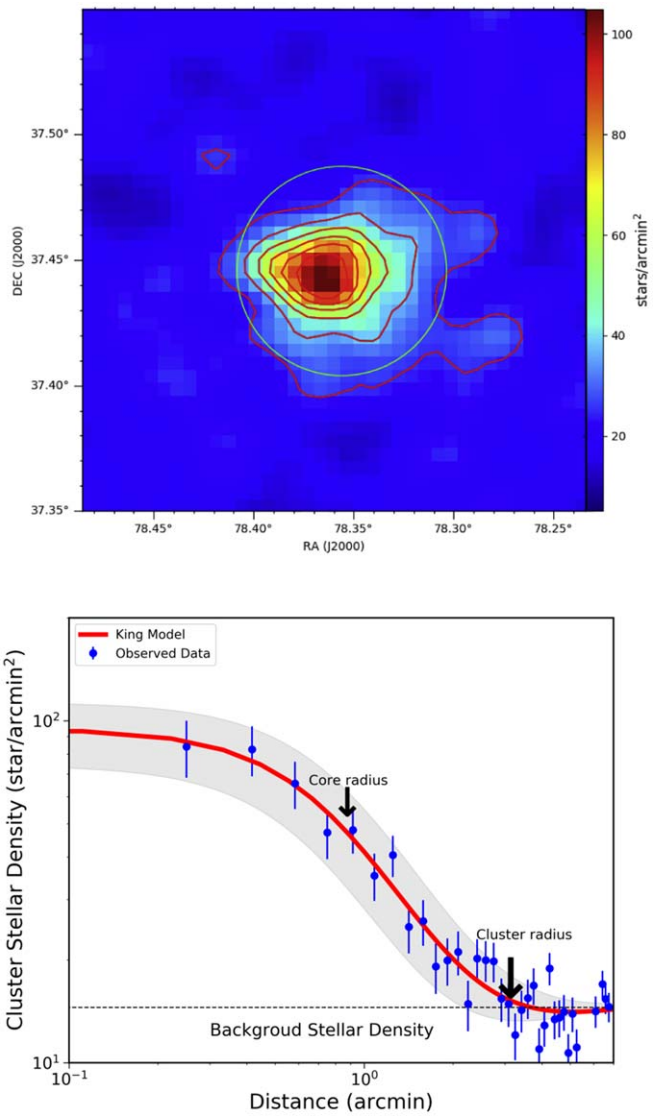

Figure 6. Upper panel: stellar surface density map of S228, made using the nearest neighbors method. The color bar represents the stellar surface density in the units of stars per arcmin^2. Contours correspond to stellar surface densities above 3σ of the mean background density, where σ is the standard deviation of the background density. The green circle represents the cluster region whose radius was obtained using the radial density profile fitting method shown in the lower panel. Lower panel: the observed stellar surface density (filled circles) of S228 as a function of radius. The horizontal line represents the mean density level of the field stars. The continuous curve shows the fitted King profile to the observed data, while the shaded area represents the 1σ error associated with the fitted profile. The error bars represent the Poisson uncertainties.

radius of 2.′6) reported in Yu et al. (2018). A circle of this estimated radius is also overplotted on the SSDM, which is in good agreement with the size of the SSDM map.

3.1.3. Distance

The distance of S228 is quite uncertain, ranging from 2.2 to 6.8 kpc (Lahulla 1985; Hunter & Massey 1990; Borissova et al. 2003; Balser et al. 2011; Kharchenko et al. 2013). With the aim to tighten the distance of the cluster, we searched for the kinematic members of the cluster using the Gaia EDR3 catalog. Figure 7 shows the proper-motion vector diagram (PVD) of relatively bright sources ($G < 18$ mag) within the cluster radius. As can be seen, there are two likely distributions in the

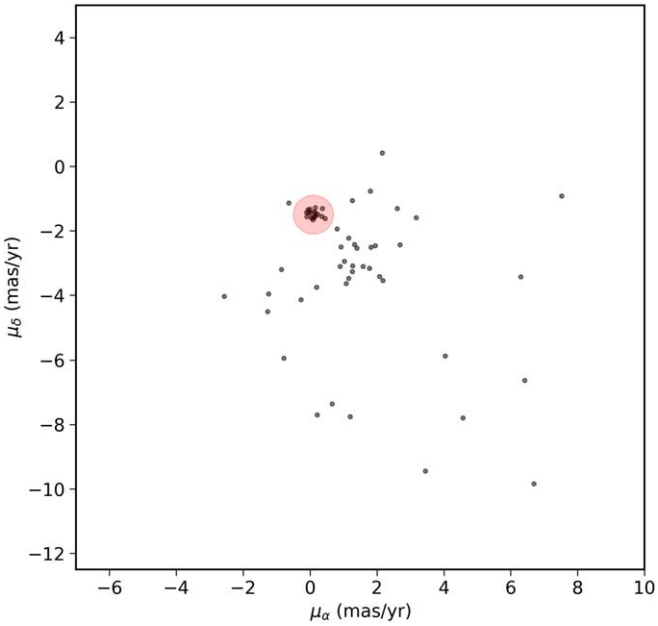

Figure 7. Proper-motion vector diagram (PVD) for all of the sources toward S228 within the cluster region. Sources distributed in the red zone represent the likely cluster members.

PVD, (i) a compact group consisting of sources of similar motion (marked with a red zone) and thus are considered as cluster members, and (ii) a loose group of sources showing scattered motion and thus are considered as field sources. A clear separation between the cluster and field star motion enables us to select member stars of S228 relatively reliably. Among the compact group sources, we reject a few outliers by keeping only those sources whose parallax (ϖ) values are within one standard deviation of the median parallax of the group and have good relative parallax uncertainties ($\varpi/\sigma_\varpi > 5$). The latter condition is primarily motivated by the fact that, if fractional parallax errors are less than about 20%, then the posterior probability distribution of parallax is nearly symmetric (Bailer-Jones 2015), hence, distance can simply be computed by inverting the parallax. With these constraints, seven sources are found to have common proper motions (PMs) and parallaxes. We find that among these sources, the ionizing source (i.e., star #1) is one of the members, while the other bright spectroscopic sources (i.e., star #2 and #3) are not members, confirming our spectroscopic membership. The PM in R.A. (μ_α), PM in decl. (μ_δ), and parallax (ϖ) values of these sources lie in the range -0.10 to 0.37 mas yr^{-1}, -1.45 to -1.30 mas yr^{-1}, and 0.28 to 0.39 mas, respectively, with medians of -0.01 ± 0.15 mas yr^{-1}, -1.40 ± 0.06 mas yr^{-1}, and 0.31 ± 0.04 mas. From the median parallax value, we estimated the distance of the cluster to be 3.2 ± 0.4 kpc, which is in agreement with the kinematic distance of 3.5 kpc, very recently derived by Mège et al. (2021) using a velocity analysis of the molecular gas associated with the region.

3.1.4. Pre-main-sequence Members

In the absence of spectroscopic or kinematic information for low-mass sources, optical and infrared color–color (CC) diagrams are often used as diagnostic tools to identify the likely pre-main-sequence (PMS) members in a star-forming region (e.g., Lada & Adams 1992; Barentsen et al. 2011). In

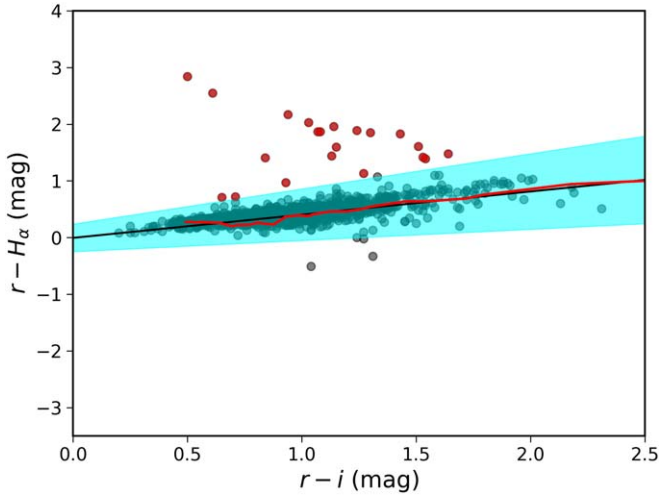

Figure 8. The IPHAS CC ($r - \mathrm{H}\alpha$, $r - i$) diagram of the point sources in the direction of the cluster. The median ($r - \mathrm{H}\alpha$) color of the field sources and 10σ limits around the median color line (blue) is shown with a shaded area. The red curve represents the synthetic MS track taken from Drew et al. (2005) corresponding to $E(B - V) = 1.0$ mag (or $A_V \sim 3.1$ mag). The filled red circles are the probable Hα excess candidates within the cluster area.

this work, we used IPHAS, UKIDSS-GPS, and Spitzer IRAC point-source catalogs above the completeness levels and employed CC diagrams to search for the PMS stars with either excess NIR emission due to the presence of a circumstellar disk or excess Hα emission due to accretion onto the stellar photosphere. The details about the CC diagrams and the identified sources are given below.

Hα Excess Emission Sources—The ($r - \mathrm{H}\alpha$) color measures the strength of the Hα line relative to the r-band photospheric continuum. Since most main-sequence stars do not show Hα emission, their ($r - \mathrm{H}\alpha$) color, which is linked to spectral type, provides a template against those objects whose ($r - \mathrm{H}\alpha$) color excess is caused by Hα emission. Moreover, in the ($r - \mathrm{H}\alpha$, $r - i$) CC space, interstellar reddening has a minimal effect on ($r - \mathrm{H}\alpha$) color, as the reddening moves only the unreddened MS track almost with a right angle to the ($r - \mathrm{H}\alpha$) color. Thus, in star-forming complexes, the ($r - \mathrm{H}\alpha$, $r - i$) diagram is often used to discern Hα emission line stars (Barentsen et al. 2011; Dutta et al. 2015). The ($r - \mathrm{H}\alpha$, $r - i$) CC diagram for the stars in the direction of S228 is shown in Figure 8. The running average ($r - \mathrm{H}\alpha$) color of the stars as a function of their ($r - i$) color is shown with a solid line, while its 10σ uncertainty is shown with a shaded area. Figure 8 shows the ($r - \mathrm{H}\alpha$, $r - i$) color of the main-sequence (MS) track taken from Drew et al. (2005) for $A_V \sim 3.1$ mag. Using this diagram, those sources with an ($r - \mathrm{H}\alpha$) color excess greater than 10σ of the average color of the stars are considered as probable emission line sources, and are marked with red circles. With this approach, we identified 21 likely Hα excess sources.

Near-infrared Excess Emission Sources—The NIR ($J - H$, $H - K$) diagram is a useful tool to identify PMS sources exhibiting NIR excess emission. However, other dusty objects along the line of sight may also appear as NIR excess sources in the CC diagram. One possible way to separate out PMS sources is to compare the CC diagram of the cluster with that of a nearby control field of the same area and photometric depth. The left panel of Figure 9 shows NIR CC diagrams of the cluster as well as that of a control field (centered at $\alpha_{2000} = 78.^\circ382386$, $\delta_{2000} = 37.^\circ17977$) located $\sim 5'$ away from the cluster field. In the NIR CC diagram, sources distributed left of the reddening vector (blue line) can be field stars, reddened MS stars, or weak-line T−Tauri stars, while sources located right of the reddening vector are considered to be PMS sources with NIR excesses (Lada & Adams 1992). As can be seen in Figure 9, compared to the cluster region, the NIR excess zone of the control field is devoid of sources, implying the presence of true NIR excess sources in the cluster region. However, in order to separate spurious sources, if any, from genuine excess sources we selected sources based on the following criteria: (i) sources with ($J - H$) colors greater than 0.7 mag because the maximum ($J - H$) color of the control field population is around 0.7 mag, and (ii) sources that fall to the right of the reddening vector with ($H - K$) color excesses larger than the uncertainties in their respective ($H - K$) colors. With this approach, we identified 14 NIR excess candidate sources within the cluster region. These sources are identified as red circles in Figure 9.

It is well known that circumstellar emission from young stars dominates at longer wavelengths, where the spectral energy distribution (SED) significantly deviates from the pure photospheric emission. We thus use Spitzer IRAC observations in combination with *JHK* data to identify additional NIR excess sources. For this purpose, we use the ($H - K$, $K - [4.5]$) CC diagram, shown in the right panel of Figure 9. It should be noted that we preferred 4.5 μm data over 3.6 μm as it is less affected by polycyclic aromatic hydrocarbon (PAH) emission, which is often present in H II region environments (Smith et al. 2010). Similar to the ($J - H$, $H - K$) analysis, we compared the distribution of cluster sources with control field sources, then selected NIR excess sources whose excess emission is greater than the error associated with the $K - [4.5]$ color of the sources and whose ($H - K$) color is greater than 0.4 mag. With this approach, we identified 25 additional candidate stars with NIR excesses. This makes 39 NIR excess sources in total.

In summary, with the above approaches, we identified 21 likely Hα emission line sources and 39 NIR excess sources. Among 21 Hα sources, 6 sources are found to have NIR excess counterparts. In total, within the cluster region, we identified 54 PMS sources. Out of the 54 PMS sources, 52 sources have optical counterparts in the Pan-STARRS1 bands and are used to derive the age of the cluster.

3.1.5. Extinction

We derived the visual extinction of the cluster using its likely OB members. Briefly, we selected OB stars from the Gaia member sources (e.g., see Samal et al. 2010) identified in Section 3.1.3 by considering only those sources whose Q value is <0.1 showing no NIR excess. This resulted in five sources out of the seven Gaia members. We then derived the ($H - K$) color excess, $E(H - K)$, of the members from the observed and intrinsic ($H - K$) colors. Since the most massive star of the cluster is an O8.5V star, we thus adopted an intrinsic ($H - K$) color of ∼0.03 mag for our analysis, which is the mean intrinsic color of O8 to B9 MS stars as tabulated in Pecaut & Mamajek (2013). We then estimated the visual extinction of the sources using the relation, $A_V = 15.9 \times E(H - K)$, adopting the extinction laws of Rieke & Lebofsky (1985). This yields a mean visual extinction $A_V = 3.3 \pm 0.6$ mag, which is in agreement with the extinction measurements of between 3.0 mag

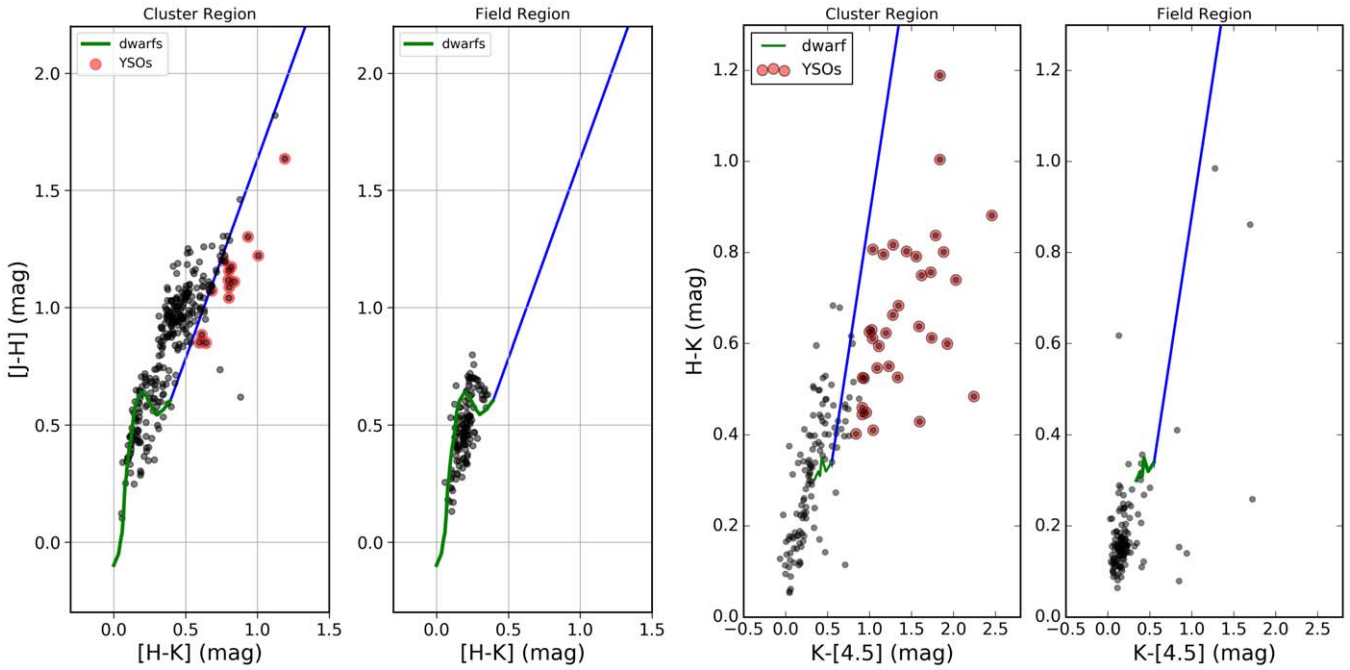

Figure 9. Left: the $(J-H, H-K)$ CC diagram for the cluster region and the control field region. The green curves are the intrinsic dwarf locus from Bessell & Brett (1988). Right: the $(H-K, K-[4.5])$ CC diagram for the cluster region and the control field region. The green curves are the intrinsic dwarf locus of late M-type dwarfs (Patten et al. 2006). In all of the plots, the blue lines represent the reddening vectors drawn from the location of an M6 dwarf, while the red circles represent likely NIR excess sources.

(Lahulla 1985) and 3.9 mag (Hunter & Massey 1990) derived for S228.

3.1.6. Age

The ages of young clusters are typically derived by fitting theoretical PMS isochrones to the low-mass contracting population. To derive the age of IRAS 05100+3723, we use the optical $(i_{P1}, i_{P1}-z_{P1})$ CMD of the PMS sources identified in Section 3.1.4 as the cluster members. We chose i_{P1} and z_{P1} bands to derive the age, as both of these bands have higher PMS counterparts over other bands of the PS1 survey. Moreover, benefits of using optical bands are that (i) it minimizes the effect of the excess emission compared to that in NIR bands, and (ii) it minimizes the effect of differential reddening, as the reddening vectors are nearly parallel to the isochrones. Figure 10 shows the $(i_{P1}, i_{P1}-z_{P1})$ CMDs of the cluster (right) as well as the nearby control field (left). In the cluster CMD, all of the sources within the cluster area and the likely PMS sources are shown with gray dots and filled circles, respectively. We find that the average A_V of the control field population is likely around 2.3 mag, which is estimated by matching a reddened theoretical zero-age main sequence (ZAMS) with the observed population. To guide our analysis, we have also plotted a ZAMS at $A_V = 2.3$ mag on the cluster CMD. A careful comparison of the distribution of the PMS sources and the control field sources on the CMD reveals that the majority of the PMS sources are redder compared to the ZAMS isochrone at $A_V = 2.3$ mag. Comparison of both of the diagrams reveals that the field population is quite significant in the direction of the cluster.

Next, we overplotted Modules for Experiments in Stellar Astrophysics (MESA) isochrones (Dotter 2016) on the CMD after correcting them for the adopted distance of 3.2 kpc and extinction $A_V = 3.3$ mag. The adopted extinction value is also found to match well with the bright PM based cluster members, implying that for the cluster, the average $A_V = 3.3$ mag is a reasonable assumption. We note that compared to the field population, the extra extinction of $A_V = 1$ mag observed in the direction of the cluster could be intrinsic to the cluster. As can be seen from Figure 10 the locations of most of the PMS sources are in the age range 0.1−10 Myr, implying that the cluster is young. We note that a small fraction of Hα emitting sources are found to be close to the field distribution. Such sources could be contaminants such as carbon stars, white dwarfs, and/or interacting binaries (for details, see Barentsen et al. 2011). In this analysis, we consider all of the PMS sources younger than 10 Myr to be most likely cluster members, because the level of accretion activity for PMS sources older than 10 Myr is expected to be very low (Williams & Cieza 2011). Then we derived the age of the individual PMS sources by comparing their location with isochrones having ages between 1 and 10 Myr with an interval of 0.1 Myr. We assigned PMS sources an age equal to the age of the closest isochrone. In this process, some sources located to the right of the 0.1 Myr isochrone are simply considered to have an age of 0.1 Myr. Doing so, we estimate the mean age of the PMS sources, and thus of the cluster, to be $\sim 2.1 \pm 1.3$ Myr. Although the smaller sample of PMS sources and variable extinction prevent us from deriving a very precise age for the cluster, our estimate agrees well with the age estimates of Borissova et al. (2003).

To ascertain our result, we further used the properties of the massive star derived in Section 3.1.1. To do so, we compared the derived $T_{\rm eff}$ and log g of the star with the MESA isochrones and stellar evolutionary tracks as shown in Figure 11. As can be seen, because of a large error in the log g value, the location of the star in Figure 11 spans a wide range of mass and age. Although accurate stellar parameters are needed to constrain the age of the star more precisely, we use the Bayesian

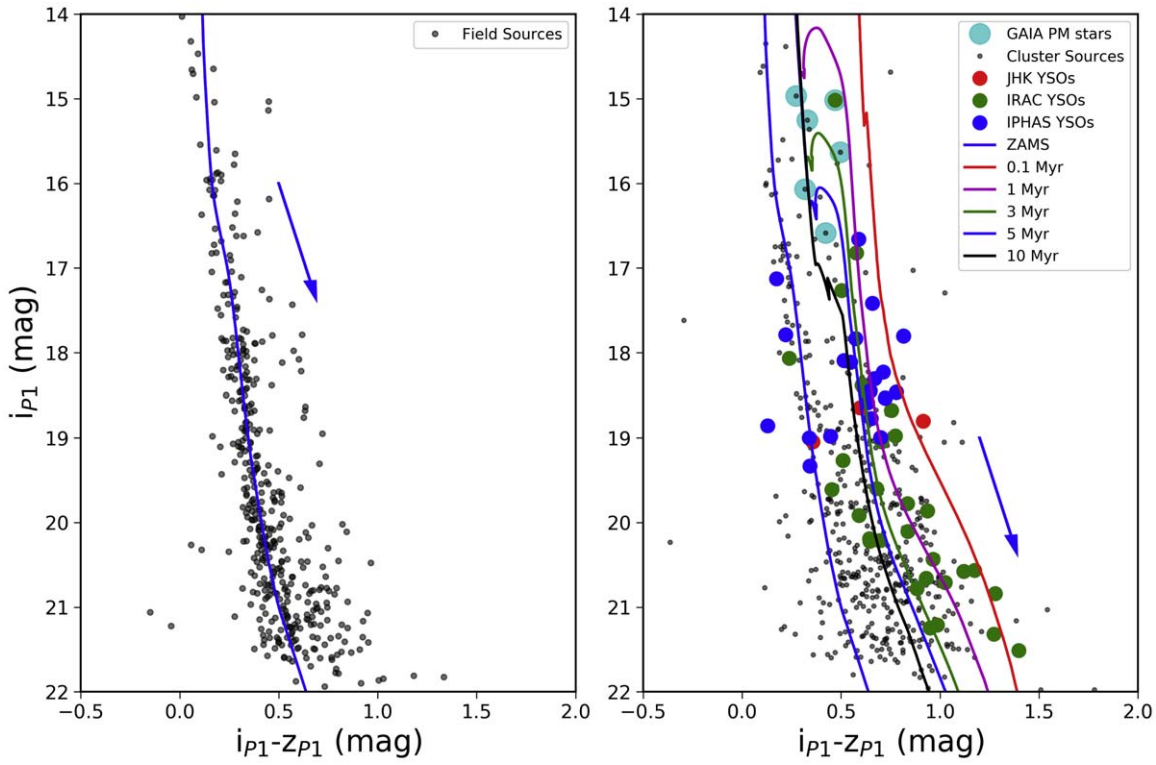

Figure 10. The optical ($i_{\rm P1}$, $i_{\rm P1} - z_{\rm P1}$) CMD of the control field (left panel) and cluster region (right panel). In the cluster CMD, the NIR excess sources identified based on *JHK* and *HK*[4.5] bands are shown by red and green circles, while the Hα excess sources are shown by blue circles, and the PM based massive members are shown by cyan circles. In the cluster CMD the PMS isochrones of ages 0.1, 1, 3, 5, 7, and 10 Myr from Dotter (2016) are shown from left to right, while the blue solid curves in both of the CMDs represent the ZAMS isochrone to guide the distribution of field stars in both of the plots. All of the PMS isochrones are corrected for a distance of 3.2 kpc and an average reddening of $A_V = 3.3$ mag. In both of the plots, the reddening vectors corresponding to $A_V = 0.5$ mag are shown by slanted arrows.

approach implemented in the isochrones package (Morton 2015) to derive the most probable age and mass of the star. The isochrones package uses the nested sampling scheme MULTINEST (Feroz et al. 2009) to capture the true multimodal nature of the posteriors. Figure 12 shows the obtained posterior probability confidence contours of mass and age with the Bayesian approach. The peak of the likelihood distribution is considered to be the most probable value, and the estimated uncertainty is determined by considering the 16th and 84th percentile values of the likelihood distribution. With this approach, we find the most probable age of the star to be $\sim$4 Myr, while the most probable mass is $\sim$20 $M_\odot$. If one takes the average uncertainty associated with the most probable value, then the age, 4.0 ± 2.7 Myr, is in reasonable agreement with the age, 2.1 ± 1.3 Myr, derived using the CMD of the low-mass stars.

With these two approaches, the average age turns out to be 3.0 ± 1.5 Myr, which we considered as the age of the cluster for further analyses. Since the cluster is associated with an H II region that is still bright in optical and radio bands, one would expect the cluster to be young. Our analysis confirms this hypothesis.

3.1.7. Mass Function and Total Stellar Mass

The stellar initial mass function (IMF) describes the mass distribution of the stars in a stellar system during birth and is fundamental to several astrophysical concepts. For a young cluster, the IMF is in general derived from the luminosity function of member stars above the completeness limit. In our case, adopting the estimated age and extinction of the cluster, we find the photometric completeness limits of our *J*, *H*, and *K* bands (see Section 2.3) correspond to mass completeness limits of 0.6 $M_\odot$, 0.6 $M_\odot$, and 0.7 $M_\odot$, respectively. We then used the *J*-band luminosity function (JLF) to derive the IMF. The selection of the *J* band is motivated mainly by the fact that the effect of circumstellar excess emission in the *J* band is minimum compared to that in the *H* and *K* bands (see Section 2.3.1), and moreover its mass sensitivity is comparable to that of these bands. Figure 13 (left panel) shows the (J, $J - H$) CMD for the cluster as well as the control field. As can be seen from the figure, the cluster region (red dots) appears to have bimodal color distributions, in which a group of redder sources with $J > 16.0$ mag are relatively well separated from a group of bluer sources. This implies that the redder sources are likely the cluster members, while the bluer sources are likely the field population in the direction of the cluster. One may also notice that compared to the ($i_{\rm P1}$, $i_{\rm P1} - z_{\rm P1}$) CMD shown in Figure 10, the (J, $J - H$) CMD shows a richer population of young sources. This could be due to the fact that infrared bands are less affected by extinction, and also young sources are intrinsically bright at longer wave bands. In the present case, we have detected 112 extra sources in the *J* and *H* bands compared to the $i_{\rm P1}$ and $z_{\rm P1}$ bands.

One can also see from the figure that the distribution of the likely field population of the cluster matches well with the distribution of the control field sources (blue dots), but appears to be slightly redder. To match the control population with the field population of the cluster, we reddened the control population with a reddening corresponding to $A_V = 1$ mag

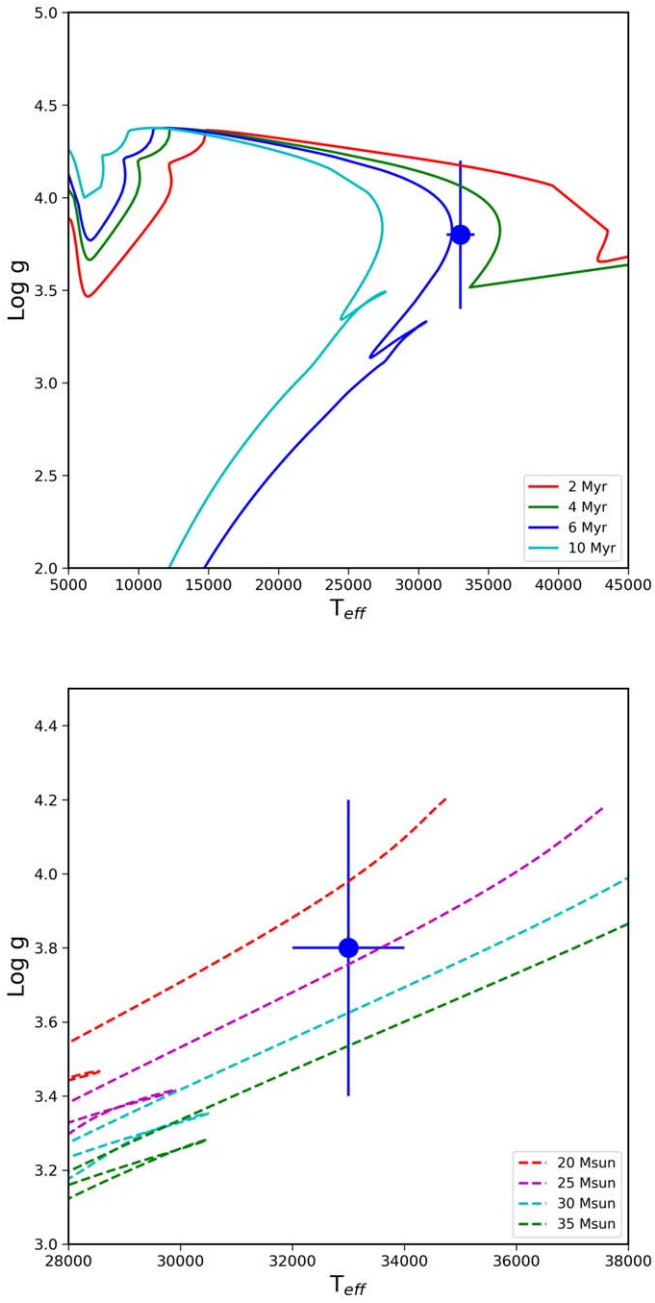

Figure 11. The (gravity (g), temperature ($T_{\rm eff}$)) diagrams for the massive star. In the upper panel, the thin solid curves are the MESA isochrones for ages 2, 4, 6, and 10 Myr, while in the lower panel the dashed lines are the evolutionary tracks for 20, 25, 30, and 35 $M_{\odot}$.

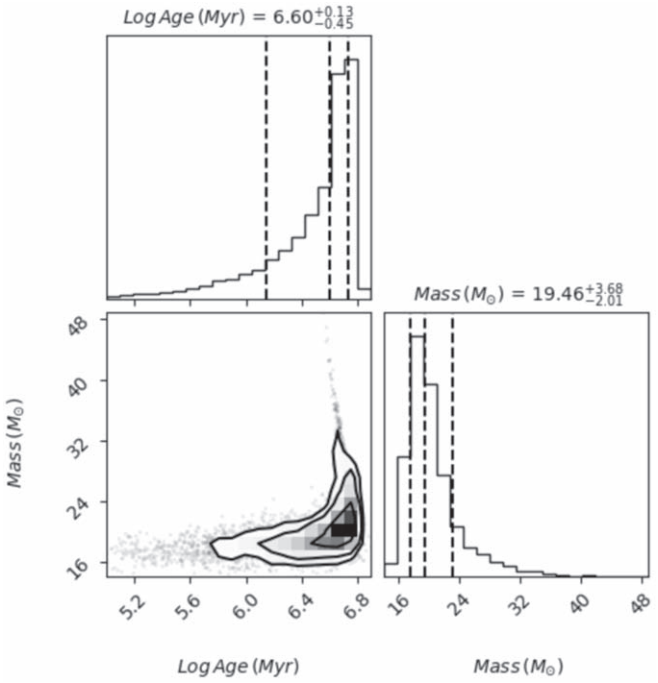

Figure 12. The lower left plot shows the posterior probability distributions of mass and age of the massive star obtained from the isochrone fitting. The upper left and lower right plots are the probability distribution histograms for the mass and age, respectively. The middle line in the histogram plots is the median value of the distribution, while the left and right lines represent the 16% and 84% percentile values, respectively.

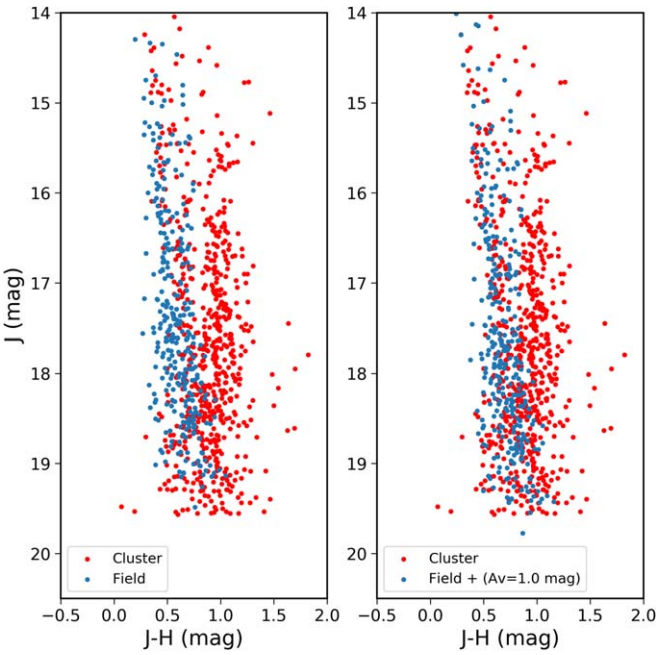

Figure 13. The (J, $J-H$) CMDs of the cluster (red dots) and the control field (blue dots). In the left panel, control field sources are plotted without any reddening correction, while in the right panel an extra reddening corresponding to $A_V = 1.0$ mag have been applied to control field sources.

(3.3−2.3 mag), as discussed in Section 3.1.6. Here, we assume that most of the field population in the direction of the cluster is in the background of the cluster. In doing so, we found that the distribution of the field population of the cluster matches well with the control population in both color and photometric depth (see Figure 13, right panel).

Figure 14 (left panel) shows the JLF of the cluster, the reddened field population, and the field subtracted cluster population. As can be seen, the JLF at the low-luminosity end, beyond $J = 18$ mag, shows a declining trend, which we attribute to the incompleteness of the data beyond $J = 17.8$ mag. We then constructed the present-day mass function (see Figure 14 (right panel)) from the field star subtracted luminosity function using the mass–luminosity relation for a 3 Myr MESA isochrone. Although the completeness limit of our J-band data keeps us from drawing any conclusions about the peak of the IMF and the shape of the IMF toward the lower-mass (M $< 0.6\,M_{\odot}$) end, in general in

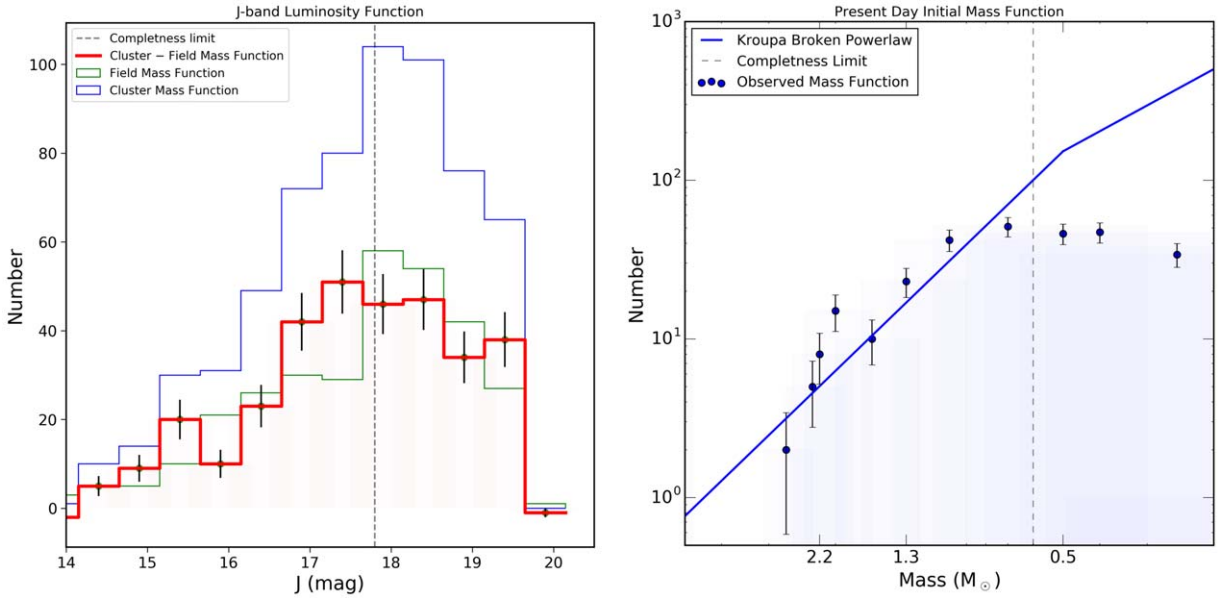

Figure 14. Left panel: the green and blue histograms represent the *J*-band luminosity functions of the cluster and control fields, respectively, while the luminosity function after correcting for the field star contamination is shown with the red histogram. The control field is reddened by $A_V = 1$ mag. In the plot, the vertical dashed line represents the ∼90% completeness limit of the *J* band, while the error bars represent the Poisson uncertainties. Right panel: present-day mass function of the cluster computed from the field star decontaminated *J*-band luminosity function, shown by dots. The 90% mass completeness limit of the data in terms of mass is shown by a vertical dashed line. The fitted power law of the observed mass function is shown by a blue line and is extended toward the low-mass end using the functional form of the mass function given by Kroupa (2001).

star clusters, the peak in the stellar distribution lies in the mass range 0.2–0.7 $M_\odot$ (e.g., Neichel et al. 2015; Damian et al. 2021). Future deeper observations of the region would shed more light on the shape of the IMF toward the lower-mass end. Nonetheless, a simple power-law fit to the data over a mass range ∼3−0.6 $M_\odot$ resulted in a slope $\alpha = -2.3 \pm 0.25$, which is comparable to the canonical value of $\alpha = -2.35$ given by Salpeter (1955) or $\alpha = -2.3$ given by Kroupa (2001) for the mass range 0.5−10 $M_\odot$. This implies that the IMF of the cluster at the high-mass end is similar to that of other Galactic clusters. We then estimated the total stellar mass of the cluster, assuming that Kroupa's broken power law (shown in Figure 14) holds true down to 0.08 $M_\odot$. Since the most massive star of the cluster is ∼20 $M_\odot$, we integrated the mass function over the mass range 20−0.08 $M_\odot$, which yields a total stellar mass of ∼510 $M_\odot$. It should be noted that using a mass function slope $\alpha = -2.33$ and integrating over the mass range 20–0.1 $M_\odot$, Borissova et al. (2003) have estimated the mass of the cluster to be 1800 $M_\odot$. For comparison, if we use a single power-law slope of −2.3 between 20−0.1 $M_\odot$, we find the total cluster mass to be ∼900 $M_\odot$. Even though our mass estimation is done over a larger area (i.e., over a 2.′5 radius), we obtained a stellar mass of less than a factor of between two and four compared to Borissova et al. (2003). The exact reason for this discrepancy is not known, however, it is worth noting that Borissova et al. (2003): (i) did not use deep control field observations for field star subtraction, instead using 2MASS data for the field population assessment, (ii) we have used a reddened control population to match the depth and color of the likely field population in the cluster region, and (iii) they used the *K*-band luminosity function for their analysis, while we use the *J*-band luminosity function. These factors could be the possible reasons for the discrepancy in the total cluster mass estimation.

The empirical relation between the mass of the most massive star ($m_{\rm max}$) of a cluster and its total mass ($M_{\rm ecl}$) is given by Bonnell et al. (2004) as:

$$m_{\rm max}^{\rm Bonnell} = 0.39 \times M_{\rm ecl}^{2/3}. \quad (2)$$

Using the Bonnell et al. (2004) relationship, we estimated that, for a cluster like IRAS 05100+3723 whose most massive star is a ∼20 $M_\odot$ star, one would expect the total cluster mass to be ∼400 $M_\odot$, consistent with our cluster stellar mass estimation. Based on our results, it can be inferred that IRAS 05100+3723 is a moderate-mass cluster (100 $M_\odot < M_{\rm cl} <$ 1000 $M_\odot$) in the classification scheme of Weidner et al. (2010).

3.2. Physical Environment and Large-scale Distribution of Gas and Dust

3.2.1. Ionized Gas Properties and Distribution

As discussed in Section 1, the cluster is associated with the H II region S228. Figure 15 shows the maps of the H II region at 150, 610, 1280, and 8700 MHz. These maps include GMRT observations at 610 MHz (beam size ∼6.″6 × 3.″4, rms noise ∼0.2 mJy beam^{-1}) and 1280 MHz (beam size ∼10″ × 8″, rms noise ∼0.4 mJy beam^{-1}), along with an 8700 MHz map (beam size ∼10.″5 × 7.″5, rms ∼0.1 mJy beam^{-1}) from the VLA archive and a 150 MHz map (beam size ∼25″ × 25″, rms ∼3.0 mJy beam^{-1}) from the GMRT TGSS.

In interferometric observations, low-level diffuse emission is often found to be missing in high-resolution and/or high-frequency observations. Despite the fact that the 150 MHz map is of low resolution, we find that compared to other bands the ionized emission at 150 MHz, however, is seen only in the central area (e.g., see Figure 16). This could be due to the lower sensitivity of the 150 MHz observations.

Normally, the free–free emission from a homogeneous classical H II region shows a rising SED with flux (S_ν) $\propto \nu^2$ at lower frequencies and an almost flat SED with $S_\nu \propto \nu^{-0.1}$ at

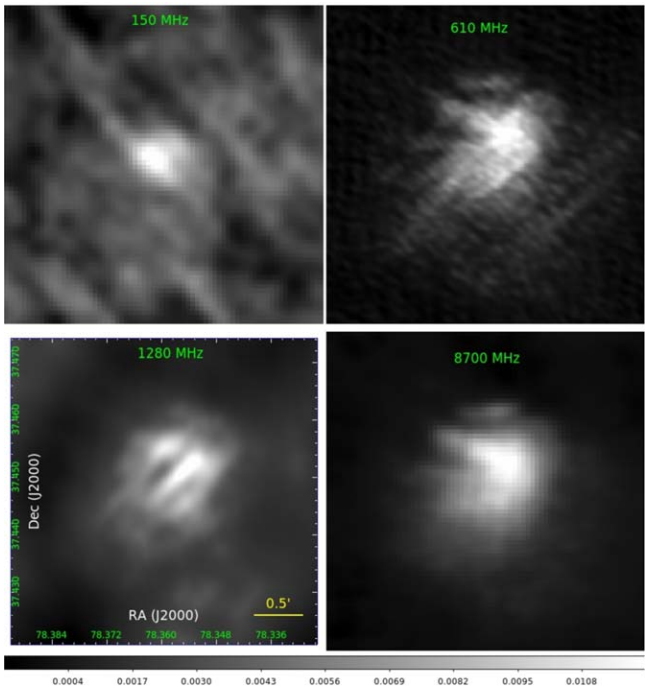

Figure 15. Radio maps of the H II region S228 at 150, 610, 1280, and 8700 MHz, showing the distribution of ionized emission at different bands. The gray-scale bar shows the intensity of radio emission in the units of mJy beam^{-1}.

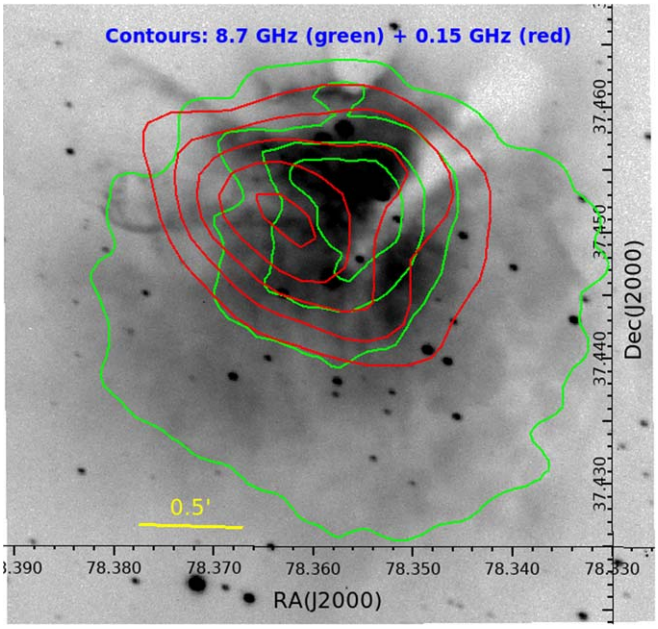

Figure 16. Comparison between emission at 8700 MHz (green contours), 150 MHz (red contours), and optical Hα emission (gray-scale background image) of the H II region. The contours are drawn above five times the rms noise of the respective maps. The 8700 MHz contour levels are at 0.0005, 0.0035, 0.0065, and 0.0095 Jy beam^{-1}, whereas the 150 MHz contours are at 0.015, 0.022, 0.029, 0.036, and 0.044 Jy beam^{-1}.

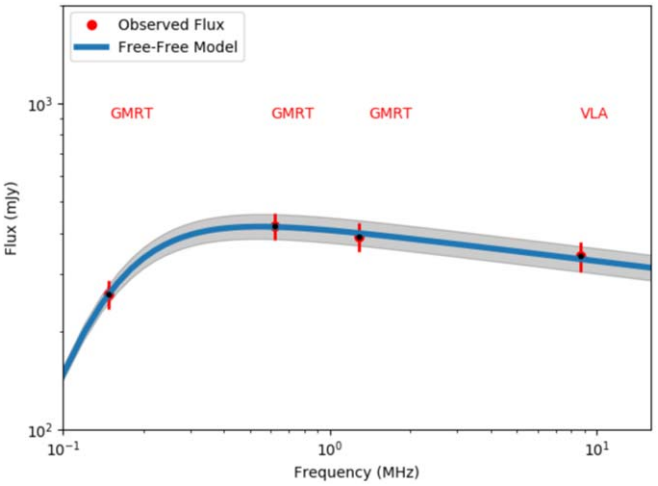

Figure 17. The SED of the H II region S228 combining flux at 150, 610, 1280, and 8700 MHz. These measurements represent the fluxes integrated over a circular area of effective radius 0.′7 (∼0.7 pc). The solid line represents the fitted free–free emission model, while the shaded area represents the 1σ uncertainty associated with the fit.

higher frequencies. However, the true behavior of S_ν with respect to ν strongly depends on the evolutionary status of the H II region and can be well constrained with thermal free–free emission modeling. Since the emission from 150 MHz is coming only from the inner region with an effective radius of ∼0.′7, we thus integrated fluxes at 610, 1280, and 8700 MHz maps over the same area as we did for 150 MHz. We note that before measuring the fluxes, we made low-resolution maps similar to the resolution of the 150 MHz map. Then, we convolved the maps to the exact resolution of the 150 MHz map. Figure 17 shows the radio spectrum of the H II region along with the thermal free–free emission model (Verschuur & Kellermann 1988) of the form:

$$S_\nu = \frac{2k\nu^2}{c^2}\Omega_s T_e(1 - e^{-\tau_{ff}}) \quad (3)$$

where the optical depth, τ_{ff}, is expressed as

$$\tau_{ff} = 0.082 \times \left[\frac{\mathrm{EM}}{\mathrm{cm^{-6}\,pc}}\right]\left[\frac{T_e}{\mathrm{K}}\right]^{-1.35}\left[\frac{\nu}{\mathrm{GHz}}\right]^{-2.1}. \quad (4)$$

In the above equations, k is the Boltzmann constant, ν is the frequency, c is the speed of light in vacuum, T_e is the electron temperature, EM is the emission measure, and Ω_s is the source solid angle. Here, we chose Ω_s to be $\frac{2r\pi}{6}$ for a circular aperture of radius r (Mezger & Henderson 1967). The free–free emission model resulted in the electron temperature $T_e \simeq 5700 \pm 400$ K and emission measure EM $\simeq 3.3 \pm 0.3 \times 10^4$ cm^{-6} pc. We then estimated the rms electron density (n_e) using the relation EM $= n_e^2 \times l$, where l is the path length and n_e is the electron density. This yielded $n_e \simeq 165 \pm 10$ cm^{-3} using the source size as the path length. We note that these values represent the average properties of the H II region over a radius of ∼0.′7, and if the H II region is clumpy, as is often the case, these values can be higher at peak positions of the clumpy structures. Nonetheless, we find that our estimates are in agreement with the electron temperature in the range 0.78 ± 0.13 to 1.02 ± 0.07 kK (Fernández-Martín et al. 2017) and electron density in the range 180 ± 10 to 222 ± 10 cm^{-3} obtained by Fernández-Martín et al. (2017) using the nebular analysis of the optical emission lines.

For optically thin free–free emission, the radio flux density is directly proportional to the flux of the ionizing photons. And as can be seen from Figure 17, the H II region is optically thin at

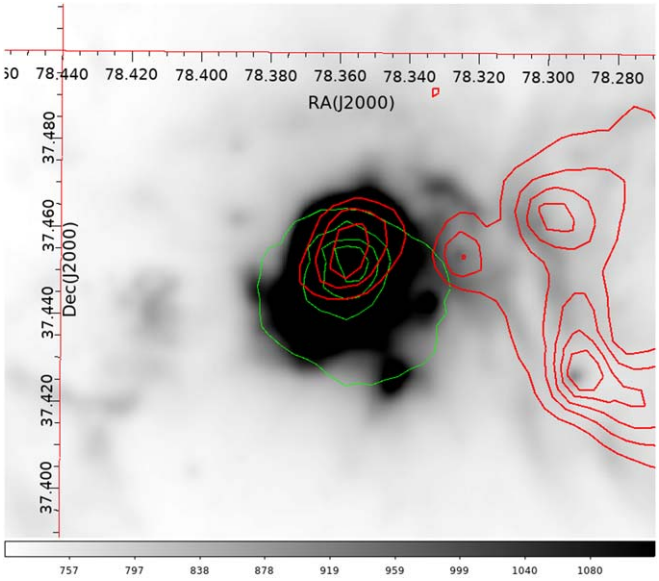

Figure 18. Image showing the distribution of WISE 12 μm (background image) emission and ionized gas emission at 8700 MHz (green contours) of S228. The red contours show the distribution of cold dust of column density greater than 3×10^{21} cm^{-2}, while the green contours reflect the 8700 MHz emission above 0.0005 Jy beam^{-1}.

high frequencies. We thus estimate the total Lyman continuum photons $N_{\rm Lyc}$ emitted per second from the ionizing star using the total integrated flux S_ν of the H II region at 8700 MHz as per the relation given in Rubin (1968)

$$N_{\rm Lyc} = 4.76 \cdot 10^{48} \left(\frac{S_\nu}{\rm Jy}\right)\left(\frac{T_e}{\rm K}\right)^{-0.45}\left(\frac{\nu}{\rm GHz}\right)^{0.1}\left(\frac{d}{\rm kpc}\right)^2 \quad (5)$$

where d is the distance to the region, while the meaning of the other terms are the same as in Equations (3) and (4). Using this relation, we estimate log ($N_{\rm Lyc}$) to be $\simeq$47.70.

In general, photodissociation regions (PDRs) are found at the surface layer of molecular clouds surrounding the H II regions. PAH molecules are strong tracers of PDRs (see Samal et al. 2007, and references therein). In this regard, WISE band 3 with an effective wavelength of $\sim$12 μm is a good tracer of PDRs, as it contains emission lines of PAH molecules (for details, see Anderson et al. 2019). We thus consider the bright diffuse 12 μm emission around the H II region to be coming from the PDR region. As can be seen from Figure 18, the 8700 MHz emission is mainly distributed within the bright PDR, implying that most of the radio emission is coming primarily from the H II region bordered by the PDR.

From spectroscopic observations, we know that the effective temperature of the massive star is $\sim$33,000 $\pm$ 1000 K; thus one would expect that the minimum log($N_{\rm lyc}$) from such a star is $\simeq$48.10 photons per second (Martins et al. 2005) considering the lower limit of the temperature. We find that this value is higher than log($N_{\rm Lyc}$) estimated from the 8700 MHz emission, implying that a fraction of the photons could have been leaked into the ISM along low-density pathways of the H II region. We discuss this point further in Section 4.3.

3.2.2. Dust Distribution and Properties

To investigate the physical conditions of dust around the S228 region, we derived column density and dust temperature maps by performing a pixel-to-pixel modified blackbody fit to the 160, 250, 350, and 500 μm Herschel images following the procedure outlined in Battersby et al. (2011) and Mallick et al. (2015). Briefly, prior to performing the modified blackbody fit, we converted all of the SPIRE images to the PACS flux unit (i.e., Jy pixel^{-1}). Then we convolved and regridded all of the shorter wavelength images to the resolution and pixel size of the 500 μm map. Next, we minimized the contribution of possible excess dust emission from each image along the line of sight by subtracting the corresponding background flux, which we estimated from a field nearly devoid of emission. Finally, we fitted the modified blackbody on these background-subtracted fluxes. For the spectral fitting, we used a dust spectral index $\beta = 2$, and the dust opacity per unit mass column density $\kappa_\nu = 0.1\,(\nu/1000\,{\rm GHz})^\beta\,{\rm cm^2\,gm^{-1}}$ as given in Beckwith & Sargent (1991), keeping the dust temperature, $T_{\rm dust}$, and the dust column density, $N(H_2)$, as free parameters.

Figure 19 shows the beam-averaged low-resolution ($\sim$36″) dust temperature and (left) dust column density maps (middle) of the S228 complex, along with the emission at Herschel 160 μm of the high column density region. As can be seen from the figure, the temperature of the dust is between 17 and 28 K, and it is distributed over a much wider area (size $\sim$10′ $\times$ 20′) than the size of the cluster (i.e., radius $\sim$2.′5). The temperature map shows an almost elongated dust distribution similar to those in bipolar H II regions (Samal et al. 2018). For example, similar to bipolar H II regions, S228 displays two dusty lobes, each with a size of $\sim$10′ ($\sim$9.6 pc) extending nearly perpendicular to a faint warm dust lane seen at the base of the lobes. The peak of the temperature map coincides with the radio continuum emission, implying the high-temperature zone is primarily created by the intense UV radiation coming from the cluster. In contrast to the temperature map, the column density map displays a lower dust column density within the bipolar H II region, but it exhibits higher column density structures with density in the range $2-7 \times 10^{21}$ cm^{-2} in the western part of the H II region. In particular, in the immediate vicinity of the H II region lies a nearly a semicircular clumpy structure with a radius of $\sim$2.8 pc and column density $>3 \times 10^{21}$ cm^{-2}. In general, molecular clumps have typical sizes of a few parsecs and are sites of active star formation. Thus, it could be a site of ongoing star formation, as column densities above $\sim 5 \times 10^{21}$ cm^{-2} are, in general, observed to be sites of recent star formation (Lada et al. 2010). In fact, we found four 70/160 μm point sources within the condensation, affirming the above hypothesis (see Figure 19 right panel). The average dust temperature of the clump is $\sim$16 K, while the average column density is $\sim 4 \times 10^{21}$ cm^{-2}. The column density map also illustrates that the clump is associated with two filamentary structures in the northwestern direction and southwestern directions, respectively. The northwestern filament is faint and narrow with a mean temperature of around 15.5 K, while the southwestern filament is slightly structured with a temperature in the range of 14.5−15.5 K.

We estimated the total mass ($M_{\rm gas}$) of the clump above a column density of $\sim 3 \times 10^{21}$ cm^{-2} using the following equation:

$$M = \mu {\rm m}_H A_{\rm pix} \Sigma {\rm H}_2 \quad (6)$$

where μ is the mean molecular weight, m$_H$ is the mass of the hydrogen atom, ΣH$_2$ is the integrated H$_2$ column density, and $A_{\rm pix}$ is the area of a pixel in cm^{-2} at the distance of the region. The above approach yields the area, mass, and density of the

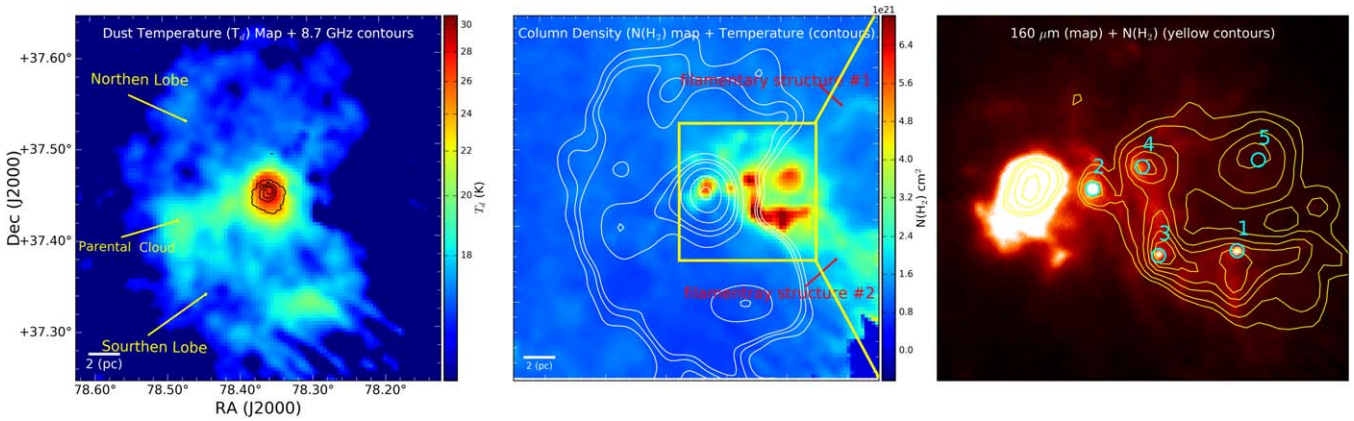

Figure 19. The left panel shows the dust temperature distribution of the S228 environment along with the distribution of ionized gas (black contours). The contour levels of the ionized gas are the same as in Figure 16. The warm dusty lobes and the heated dust of the central parental cloud are also marked. The middle panel shows the dust column density distribution along with the dust temperature contours at 17.2, 16.4, 17.6, 18.4, and 19.0 K. Two filamentary structures attached to the western clump are also marked. The right panel shows the zoomed view of the western clump. The background image is the Hershel 160 μm map and the yellow contours correspond to the dense gas above a column density of 3×10^{21} cm^{-2}. The CUTEX identified compact sources are labeled #1 to #5.

clump of $\sim$28 pc^2, $\sim$2700 $M_\odot$, and $\sim$350 cm^{-2}, respectively. We find that the properties of the clump are similar to those of the nearby Ophiuchus star-forming region, which is one of the youngest (age $\sim$1 Myr) and closest (distance $\sim$125 pc) star-forming regions, having a size of $\sim$29 pc^2 and a mass of $\sim$3100 $M_\odot$ (Dunham et al. 2015).

The stability of a clump against gravitational collapse can be evaluated using the virial parameter (Kauffmann et al. 2013)

$$\alpha = 1.2\left(\frac{\sigma_v}{\text{km s}^{-1}}\right)^2\left(\frac{R_{\text{eff}}}{\text{pc}}\right)\left(\frac{M}{10^3 M_\odot}\right)^{-1} \quad (7)$$

where σ_v is the one-dimensional velocity dispersion, R_{eff} is the effective radius, and M is the mass of the clump. In general, $\alpha < 1$ is suggestive of collapsing clumps, while $\alpha > 2$ is suggestive of dissipating clumps, and $\alpha \sim 1-2$ describes a clump that is in approximate equilibrium. However, the external pressure confined clumps with $\alpha \leqslant 2$ are also found to be bound and can live longer with respect to the dynamical timescale (Bertoldi & McKee 1992). In the present case, using $\sigma = 1.3$ km s^{-1} estimated over the clump area from the ^{13}CO map (discussed in Section 4.3), we find $\alpha \sim 1.6$, implying that clump may still be bound.

3.2.3. Herschel Compact Sources and Properties

From the right panel of Figure 19, it appears that the western clump has been fragmented into five compact structures (marked with numbers #1 to #5), four of which (sources #1 to #4) are protostellar, as each of them is associated with a 70/160 μm point source, while source #5 is not associated with any point-like source and thus is likely a prestellar source. The presence of 70/160 μm point sources within column density peaks suggests that fresh star formation is happening at the western border of the nebula.

In order to understand the properties and evolutionary status of the 160 μm point sources, we extracted their far-infrared fluxes between 70 and 500 μm using the CUrvature Thresholding EXtractor (CUTEX) software described in Molinari et al. (2011). The CUTEX was specifically developed to optimize the source detection and extraction in a spatially varying background such as the emission seen in the Herschel maps of star-forming environments (e.g., Molinari et al. 2011). In order to estimate the envelope temperatures of the identified point sources, we fitted the observed fluxes at 70, 160, 250, and 350 μm with the modified blackbody model. Fluxes at 500 μm have been excluded, owing to the low resolution of the 500 μm beam. This is done in order to avoid bias in the fitting procedure due to the overestimation of fluxes at 500 μm because of source confusion and the inclusion of excess background emission. We also adopted a 20% error in flux values instead of formal photometric errors, in order to avoid any possible bias caused by an underestimation of the flux uncertainties. We fitted the modified blackbody of the form, $S_\nu = A\,\nu^\beta B_\nu(T_{\text{dust}})$, where S_ν is the observed flux distribution, A is a scaling factor, $B_\nu(T_{\text{dust}})$ is the Planck function for the dust temperature T_{dust}, and β is the dust emissivity spectral index. A sample SED is shown in Figure 20 for $\beta = 2$.

Having derived dust temperature, we then determined the total mass (gas + dust) of the envelope from the dust continuum flux, S_ν, using the following equation:

$$\text{Mass} = \frac{S_\nu\, Rd^2}{\kappa_\nu\, B_\nu(T_{\text{dust}})} \quad (8)$$

where d is the distance, R is the gas-to-dust ratio and is considered to be 100, and κ_ν is the dust mass opacity. We used the same dust opacity law as in Section 3.2.2. We also estimated bolometric luminosities of the sources by integrating SEDs between 2 and 1000 μm. We note that, since we have not taken into account the wavelength dependence of β, the uncertainty in the mass can be a factor of two, as discussed in Deharveng et al. (2015). Moreover, if the compact structures contain multiple point sources that are unresolved at Herschel bands, the derived mass and luminosity can be even more discrepant. Nonetheless, taking these properties of the sources at face value, we infer their likely evolutionary status by plotting them on the M_{env}–L_{bol} diagram. Figure 21 shows the M_{env}–L_{bol} diagram of the sources along with the evolutionary tracks of protostellar objects from André et al. (2008). The figure also marks the zones of Class 0 and Class I sources. As can be seen, all of the sources lie in the Class 0 zone of the plot and the evolutionary tracks in the plot indicate that these

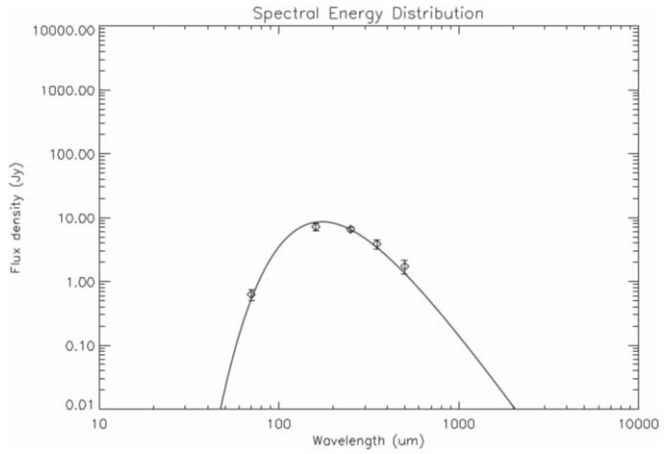

Figure 20. The SED of the embedded source #4. The circles denote the observed flux values. The black solid curve shows the graybody fit to the data points, between 70 and 350 μm.

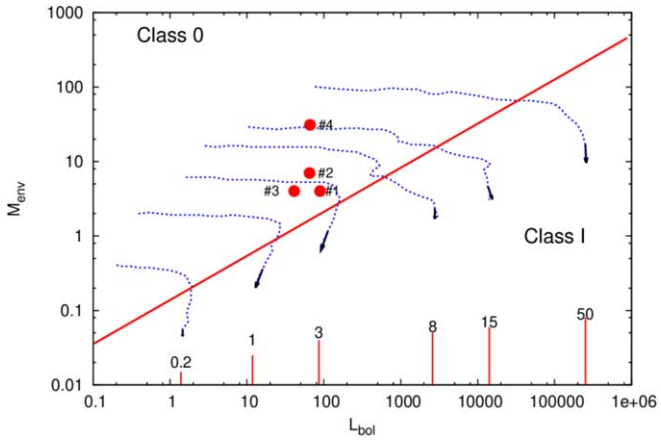

Figure 21. The (L_{bol}, M_{env}) diagram of the candidate protostars detected in the western clump (ID numbers are the same as in Figure 19). The dashed blue lines represent the evolutionary tracks from André et al. (2008). Evolution proceeds from the upper left to the lower right (indicated by arrows at the end of each track). The final stellar masses of these tracks, in solar units, are given above the vertical lines. The slanted red line corresponds to the location where 50% of the initial core mass is converted into stellar mass (Bontemps et al. 1996; André et al. 2000).

objects would evolve into stars in the mass range ∼3–15 $M_{\odot}$. This implies that the condensation is possibly a site of low- to intermediate-mass star formation.

4. Discussion

4.1. Gas Removal and Dynamical Status of the Cluster

Stellar feedback plays an important role in the removal of gas from star clusters, and subsequently cluster members dissolve completely into the Galactic field (Lada & Lada 2003). It is suggested that by comparing the age of a star in the cluster with its crossing time (T_{cr}) one can distinguish expanding clusters from bound clusters. According to Gieles & Portegies Zwart (2011), $\frac{T_{cr}}{\text{Age}} \sim 1$, separates bound clusters ($T_{cr} <$ Age) from the unbound associations ($T_{cr} >$ Age). The general definition of T_{cr} ($=2R_H/\sigma$) includes half mass–radius (R_H) and the rms velocity dispersion (σ) of the member stars (Binney & Tremaine 2008). Since we do not have velocity measurements of stars, we thus use the expression $T_{cr} = 2.8(R_V^3/GM)^{1/2}$ to estimate the crossing time, where M is the total mass of the system, G is the gravitational constant and is $\simeq$0.0045 pc^3 $M_{\odot}^{-1}$ Myr^{-1}, and R_V is the virial radius of the cluster (Weidner et al. 2007; Gieles 2010). The latter is related to the R_H as $R_V = 1.25 \times R_H$. We made an approximate estimate of the R_H from the cluster center as the radius where the star counts above the photometric completeness level is exactly half of the total number of stars within the cluster radius, and it turns out to be 1.07 pc. We assume that the mass of each star is roughly ∼0.5 $M_{\odot}$, based on the fact that the mass distribution of stars in young clusters peaks somewhere between 0.2 and 0.7 $M_{\odot}$ (Damian et al. 2021). Using this approach, we estimated T_{cr} to be ∼3 Myr, implying that the cluster is probably marginally bound or in its initial stage of expansion, considering its age of ∼3 Myr. It is worth noting that recently Kuhn et al. (2019) studied a sample of 28 clusters and associations with ages ∼1–5 Myr using PM measurements from Gaia DR2 and revealed that at least 75% of these systems are expanding.

4.2. Comparison to Other Young Clusters

Lada & Lada (2003) examined a sample of young embedded clusters within 2 kpc from the Sun with deep NIR observations and have tabulated their properties. We find that IRAS 05100 +3723 is more massive than the majority of the nearby embedded clusters, except for the Orion Nebula Cluster (ONC). The ONC is one of the nearest (∼450 pc), young (∼2 Myr), massive (≥1000 $M_{\odot}$) clusters, and hosts four massive stars of spectral type between B0 and O7 (for details, see Panwar et al. 2018, and references therein). Compared to the ONC, IRAS 05100+3723 is a slightly more evolved (age ∼3 Myr) and less massive (mass ∼500 $M_{\odot}$) cluster and hosts only a single massive star of spectral type O8.5. We find that in terms of mass, age, and size, the studied cluster resembles the cluster Stock 8, studied by Jose et al. (2017). Stock 8 is a young cluster of age ∼3 Myr with the most massive star being a star of spectral type between O8 and O9 and a total stellar mass of ∼580 $M_{\odot}$. We also find that IRAS 05100+3723 lies well below the mass–radius relation (mass $\propto r^{1.67}$) given by Pfalzner et al. (2016), derived for embedded clusters. This could be due to the fact that the cluster is possibly expanding and dispersing into the Galactic ISM. As a result, the cluster is not compact anymore, while embedded clusters are, in general, bound and compact systems. In fact, we find that IRAS 05100+3723 lies between embedded and loose clusters in the radius−age plane of Pfalzner & Kaczmarek (2013). However, the total A_V in the direction of the cluster is 3.3 mag, but extinction intrinsic to the cluster is only $A_V \sim 1$ mag, which also points toward the fact that the cluster is probably no more an embedded cluster.

4.3. Star Formation Processes and Activity in the Complex

4.3.1. Cloud Structure, Cluster Formation, and Leaking Fraction of the Ionized Gas

Figure 22 shows the ^{13}CO gas distribution in the complex, along with warm and cold dust distributions derived from the temperature and column density maps. The ^{13}CO intensity map was made using the observations taken with the FCRAO telescope at a spatial resolution of ∼45″ and a velocity resolution of ∼0.25 km s^{-1} (provided by Mark Heyer in a private communication). In the ^{13}CO spectrum, two velocity components are found in the direction of S228, as shown in

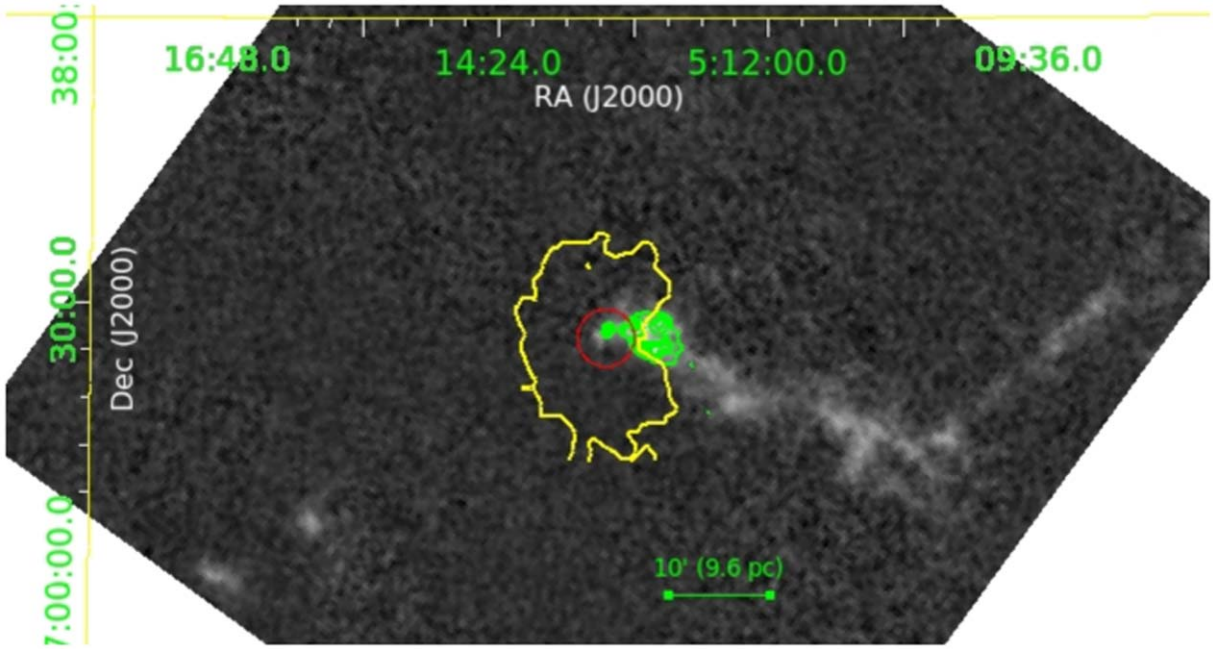

Figure 22. The image shows the distribution of ^{13}CO intensity in gray scale. The outer boundary of the Herschel dust temperature map is shown with a yellow contour with $T_d = 17.2$ K. The extent of the cluster is shown with a red circle. The Herschel column density contours above density 3×10^{21} cm^{-2} (in the direction of the western clump) are shown in green. The contour levels are the same as in the right panel of Figure 19.

Figure 23. We obtained the moment maps (i.e., intensity, velocity, and velocity dispersion maps) of S228 region using its velocity component in the range -13.5 to -3.5 km s^{-1}, the velocity range corresponding to S228 (e.g., Chen et al. 2020). As shown in Figure 22, the distribution of the ^{13}CO intensity suggests that the cluster lies at the end of a filamentary cloud. It is generally hypothesized that star-forming clouds collapse to lower-dimensional structures, producing first sheets and then filaments (Lin et al. 1965; Burkert & Hartmann 2004; Gómez & Vázquez-Semadeni 2014; Naranjo-Romero et al. 2020). Simulations show that such clouds experience highly nonlinear gravitational acceleration as a function of position, causing the material to pile up near the cloud edge, forming a young cluster like Orion (e.g., Burkert & Hartmann 2004; Hartmann & Burkert 2007; Heitsch et al. 2008).

From the ^{13}CO moment 1 map, we find that the V_{LSR} of the ^{13}CO molecular gas in the zone of the ionized gas is ~ -5.5 km s^{-1}, while the V_{LSR} of the ionized gas lies in the range -9.4 to -13.6 km s^{-1} (Israel 1977; Chen et al. 2020). The mean velocity of the ionized gas differs from that of the molecular gas by 4−8 km s^{-1}, implying that the ionizing gas is possibly streaming away from the cloud. This behavior is typical for H II regions where massive stars form near the very edge of a molecular cloud (Tenorio-Tagle 1979) or in the center of a flat or sheet-like cloud (Bodenheimer et al. 1979), resulting in an easy flow of the ionized gas along the low-density paths of the parental cloud.

Since the morphology of the warm dust is more like the morphology of a bipolar H II region, we thus hypothesized that the H II region might have formed at the very end of a sheet-like or flattened cloud containing a central filament as advocated in Deharveng et al. (2015). In such clouds, density along the equatorial axis is expected to be high, whereas it is expected to be low in the polar directions. Considering that the ionized gas is streaming away from the filamentary cloud at a minimum velocity of $\sim$5 km s^{-1}, one would expect that the ionized gas would reach $\sim$15 pc in 3 Myr (i.e., the age of the cluster) from its original location. This is comparable with the projected size, $\sim$10 pc, of the warm dusty lobes seen in the temperature map. This also suggests that a fraction of the ionizing photons could have leaked into the surrounding ISM, heating the dust up to several parsecs. Comparing the Lyman continuum photons expected from the ionizing star of the H II region with the observed Lyman continuum photons derived from radio observations within the bright PDR zone, we find that approximately 60% of the Lyman photons likely have escaped from the H II region into the diffuse ISM during the lifetime of the star. If we consider the uncertainty in the estimation of temperature and density of the ionized gas, then also the escape fraction is in the range of 40%−50%. Our

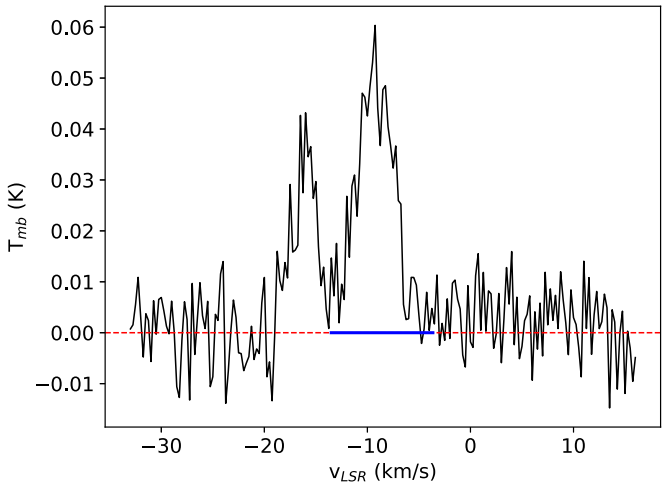

Figure 23. Average ^{13}CO spectrum observed toward the S228 complex. The red and blue lines indicate the entire velocity range and the velocity range associated with the S228 complex.

estimated escape fraction is in good agreement with the values found for other H II regions (e.g., Oey & Kennicutt 1997; Pellegrini et al. 2012). We note that the escape fraction also strongly depends on the age of the Lyman photon emitting source, and on the structure and geometry of the medium (Bodenheimer et al. 1979; Yorke et al. 1982; Howard et al. 2017); thus, it may vary from region to region.

4.3.2. Compression and Confinement of Cold Gas and Formation of Dense Clump

Figure 22 shows that the western clump (shown by green contours) lies close to the H II region. The clump displays a bow-like morphology with its apex facing the H II region, as found in numerical simulations of H II regions expanding into collapsing molecular clouds (e.g., Walch et al. 2015). This suggests that the overpressured expanding H II region possibly has compressed and pushed the western clump to its present shape. To evaluate the degree of interaction between the H II region and the clump, we evaluated various average pressures within both regions using the equations given below. We estimated pressure due to ionized gas of the H II region using the following relation:

$$P_{\rm H\ II} = \sqrt{\frac{3Q_{\rm H}}{4\pi\alpha_{\rm rec} r^3}}\,kT \approx 10^{-9}\left(\frac{Q_{\rm H}}{2\times10^{49}\ {\rm s^{-1}}}\right)^{1/2}\left(\frac{0.72\ {\rm pc}}{r}\right)^{3/2}\ {\rm dyn\ cm^{-2}} \quad (9)$$

where r is the radius, $Q_{\rm H}$ is the Lyman continuum photon responsible for the ionization of the H II region, and $\alpha_{\rm rec}$ is the recombination coefficient (for details, see Equation (6) of Murray 2009). $Q_{\rm H}$ is taken to be $\sim5.1\times10^{47}$ photons per second, while for the clump it is assumed to be zero as no hyper or ultracompact H II regions are present in our high-resolution 8700 MHz image. We estimated radiation pressure using the following relation:

$$P_{\rm rad} = L/4\pi cr^2 = 4.4\times10^{-15}\left(\frac{L}{L_\odot}\right)\left(\frac{r}{\rm pc}\right)^{-2}\ {\rm dyn\ cm^{-2}} \quad (10)$$

where we adopted the ionizing star of the H II region as the dominant source of stellar luminosity (L), while in the clump the $L_{\rm bol}$ of the most massive protostar is adopted as a proxy for stellar luminosity. We then estimated the turbulent pressure using the following relation:

$$P_{\rm turb} = \rho\sigma_{\rm nt}^2 = 4.7\times10^{-14}\left(\frac{n}{\rm cm^{-3}}\right)\left(\frac{\sigma_{\rm nt}}{\rm km\ s^{-1}}\right)^2\ {\rm dyn\ cm^{-2}} \quad (11)$$

within the H II region and the clump, where ρ is the mass density, n is the particle density, and

$$\sigma_{\rm nt} = \sqrt{\sigma_{\rm obs}^2 - \sigma_{\rm th}^2} \quad (12)$$

is the nonthermal velocity dispersion of the gas. Assuming a Gaussian distribution of the line profiles, $\sigma_{\rm obs}$ and $\sigma_{\rm th}$ can be estimated from line widths (ΔV) using

$$\sigma_{\rm obs} = \frac{\Delta V_{\rm obs}}{2.35}\ \text{and}\ \sigma_{\rm th} = \frac{\Delta V_{\rm th}}{2.35}. \quad (13)$$

For the ionized gas within the H II region, we used the observed line width of the hydrogen radio recombination (RRL) line from Chen et al. (2020), while for the clump we used the line width of the ^{13}CO line within the clump area. For the molecular gas, we used the expression $\Delta V_{\rm th} = \sqrt{\frac{8\ln 2kT}{m_{\rm co}}}$, where k is the Boltzmann constant, T is the kinetic temperature of the molecular gas, and $m_{\rm co}$ is the mass of ^{13}CO molecule in amu. For the ionized gas, we used the expression $\Delta V_{\rm th} = 21.4\sqrt{\frac{T_{\rm e}}{10^4K}}$ for the hydrogen atom (Garay & Lizano 1999), where $T_{\rm e}$ is the electron temperature. Lastly, we estimated thermal pressure using the equation:

$$P_{\rm therm} = 2nkT = 2.8\times10^{-16}\left(\frac{n_e}{\rm cm^{-3}}\right)\left(\frac{T}{K}\right){\rm dyn\ cm^{-2}} \quad (14)$$

where we used the mean density and mean temperature of the ionized gas and cold dust. Doing so, we estimated the total pressure within the ionized region

$$P_{\rm ionized} = P_{\rm H\ II} + P_{\rm rad} + P_{\rm turb} + P_{\rm therm} \quad (15)$$

to be $\sim4.5\times10^{-8}$ dyn cm^{-2}, and the total pressure within the clump

$$P_{\rm clump} = P_{\rm rad} + P_{\rm turb} + P_{\rm therm} \quad (16)$$

to be $\sim2.3\times10^{-9}$ dyn cm^{-2}, implying that the H II region must still be compressing the clump, and as a result the clump may be under external pressure confinement. However, since the typical average pressure of the ISM is in the range 10^{-11}–10^{-12} dyn cm^{-2} (Bloemen 1987; Draine 2011), we hypothesize that the H II region must be expanding more rapidly into the ISM. In the present case, the expansion may be occurring more preferentially in the direction perpendicular to the plane of the cloud, and, as a result, we observe warm dusty bipolar lobes.

The Herschel column density map shows (see Section 3.2.2) that the clump is located at the junction of two filamentary structures, while in the large-scale ^{13}CO map, the clump seems to be located at the end of a long L-shaped filamentary structure. This long filamentary structure corresponds to the southwestern filament seen in the Herschel image. The nonvisibility of the small northwestern filament in the ^{13}CO map could be due to the lower sensitivity of the ^{13}CO map. We note that the small-scale filamentary structures can be generated due to the self-gravity of the clump. Nonetheless, the situation is very similar to that of several other star-forming regions where massive clumps have been found at the merger or convergence point of filaments (e.g., Myers 2009; Schneider et al. 2012; Kumar et al. 2020) or at the end of a large-scale filament due to edge collapse (e.g., Burkert & Hartmann 2004; Pon et al. 2011; Yuan et al. 2020). The large-scale velocity gradients along the filaments have often been interpreted as signatures of mass flow toward star-forming clumps as a consequence of the longitudinal collapse of the filaments (Kirk et al. 2013; Ryabukhina et al. 2018; Dutta et al. 2018). Although the structure of the filament is not very

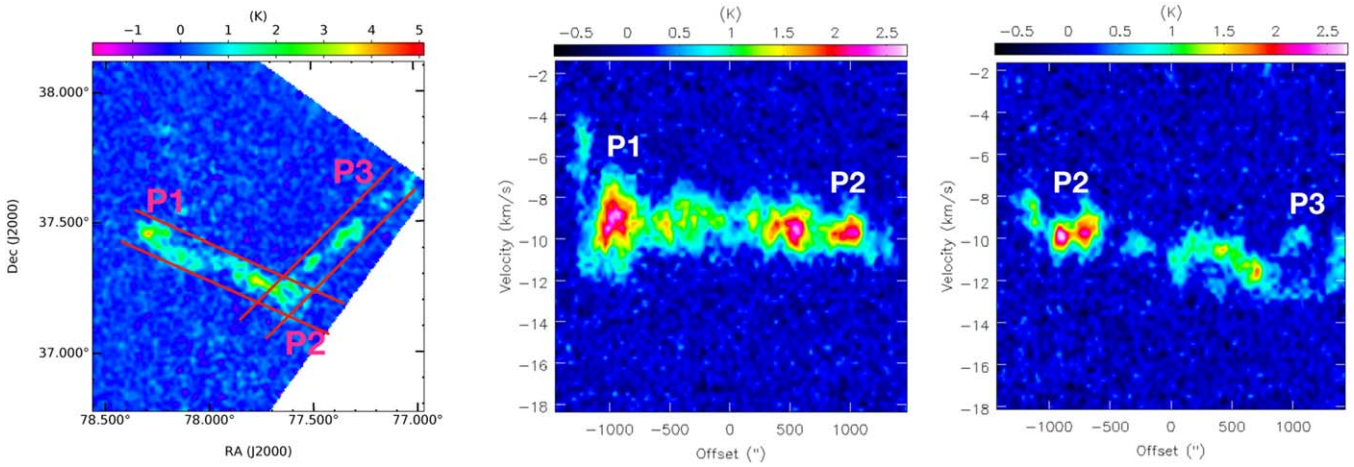

Figure 24. Position−velocity (PV) maps along the long axis of the L-shaped filament. The left panel shows the ^{13}CO intensity map of the filament in Galactic longitude and latitude coordinates, the middle panel shows the PV map of the P1−P2 filament, and the right panel shows the PV map of the P2−P3 filament.

smooth, which could be due to star formation activity at multiple locations of the filament, as the filament is presumably older than 3 Myr (i.e., the age of the cluster), we searched for signatures of an underlying large-scale flow (i.e., signatures of velocity gradient) along the filament's long axis in the position–velocity (PV) map. Figure 24 shows the PV maps of the filament, extracted along its spine. To extract the PV maps, we divided the L−shaped filament into two parts (P1−P2 and P2−P3) as marked in Figure 24 (left panel). Figure 24 (middle panel) and Figure 24 (right panel) show the PV maps of P1−P2 and P2−P3, respectively. In PV maps, the velocity gradient in P1−P2 is weaker compared to the one observed for the P2−P3 region. Overall, the velocity gradient in the whole filament is ∼0.05 km s^{-1}. This weak velocity gradient could be due to the possibility that, because the filament is ∼3 Myr old (cluster age), star formation along the filament has already distorted its gas kinematics and also has changed the location of the star-forming potential and thus the kinematics at smaller scales during its evolution (e.g., see discussions in Peretto et al. 2014). Nonetheless, the velocity gradient (i.e.,∼0.1 km s^{-1} pc^{-1}) observed within P2−P3 is comparable to that of some of the large-scale filaments such as IRDC G035.39–00.33 (∼0.2 km s^{-1} pc^{-1}; Sokolov et al. 2017) and the W33 filamentary system (0.3–0.1 km s^{-1} pc^{-1}; Liu et al. 2021). This points to the fact that the filament has likely been dynamically active for a few Myr, and thus might have supplied cold matter to the cluster location. However, high-resolution spectral observations of the filament close to the clump location will be essential to better understand the filamentary flow.

4.3.3. Second-generation Star Formation

In the filamentary environment, numerical simulations by Fukuda & Hanawa (2000) suggest that the expansion of an H II region can generate sequential waves of star-forming cores along the long axis of the filament on either side of the H II region. This has been particularly observed in bipolar H II regions, which are thought to be formed due to an anisotropic expansion of the H II region in a flat or sheet-like cloud containing filaments (Deharveng et al. 2015; Samal et al. 2018). Indeed, Samal et al. (2018), from the analysis of a sample of bipolar bubbles, found that the most massive and compact clumps with signatures of massive star formation are always located at the waist of the bipolar bubbles, and they argue that these massive clumps are the possible sites of second-generation massive- to moderate-mass star formation. Eswaraiah et al. (2020), using magnetic field geometry and strength, and comparing various pressure components, showed that the evolution and star formation of the clumps at the waists of bipolar H II regions are indeed strongly influenced by the H II region feedback.

The morphology of the S228 in WISE 12 μm and Herschel temperature map appears to be bipolar with two lobes extending nearly perpendicularly to a faint dust lane located at the bases of the lobes. At the western waist of the bubble lies a clump whose mean temperature and mean column density are 16 K and ∼4×10^{21} cm^{-2}, respectively, which are conducive for the process of star formation (Lada et al. 2010; Eden et al. 2019).

Within this dense clump, as discussed in Section 3.2.3, several Class 0/I protostars and a starless core have been identified. The fact that the age of Class 0/I sources is of the order ∼10^5 yr (Evans et al. 2009), these sources are located in a clump that lies at the junction point of the H II region and filament, and the clump is under the influence of a ∼3 Myr old H II region, all together suggest that these protostars are the likely second-generation stars of the complex.

5. Summary

In order to understand the formation of young massive clusters and their feedback effects on the parental cloud, we investigated the young cluster IRAS 05100+3723 and studied its environment using multiwavelength data sets.

Our findings conclude that IRAS 05100+3723 is an intermediate-mass (mass ∼500 $M_\odot$) young cluster formed around 3 Myr ago at the very end of a long filamentary cloud. We find that the massive star of the cluster has created an H II region of size ∼2.7 pc and temperature ∼5700 K. However, it has heated the dust out to several parsecs and the distribution of the warm dust on a large-scale resembles a bipolar H II region. This implies that the parental cloud could be sheet-like or flattened in nature, containing a central filament as suggested by Deharveng et al. (2015) for molecular clouds that host bipolar H II regions.

Although high-resolution kinematic studies of the filament are needed, we nonetheless hypothesized, based on the evidence found in Sections 4.3.1 and 4.3.2, that the formation

of the cluster (and the H II region) is likely due to the edge or end-dominated global collapse of the filament as advocated in Burkert & Hartmann (2004) and Pon et al. (2011), from which the formation of the western clump followed. We suggest that the latter is either induced or facilitated by the compression of the expanding H II region (Section 4.3.2) onto the inflowing filamentary material.

Inside the clump, we observed several far-infrared point sources of class 0/I nature. We suggest that these sources are the second-generation stars of the complex, as such sources are absent in the vicinity of the ionizing star of the H II region (see Section 3.2.3), they are significantly younger (age $\sim 10^5$ yr) than the age of the H II region (age $\sim$3 Myr), and they occupy a distinct location (i.e., at the interaction zone of the H II region and filament) compared to optically visible stars. We hypothesize this scenario may be applicable to star formation at the border of several H II region−filament environments and may be an efficient process for forming second-generation stars in molecular clouds. Future high-resolution studies of a larger sample of young H II region−filament environments would be helpful to support our hypothesis.

We thank the anonymous referee for providing valuable comments and suggestions that improved the paper. This paper, in part, is based on observations made with MRES mounted on TNT at the Thai National Observatory (program ID C06_024). TNT is operated by the National Astronomical Research Institute of Thailand (Public Organization). We acknowledge Mark Heyer for sharing FCRAO ^{13}CO observations. This research has made use of the SIMBAD database, operated at CDS, Strasbourg, France. Herschel is an ESA space observatory with science instruments provided by European-led Principal Investigator consortia and with important participation from NASA. The Gaia space mission is operated by the European Space Agency (ESA). This publication uses data from UKIDSS. This work, in part, uses data from the Pan-STARRS1 (PS1) surveys. We acknowledge data obtained as part of the INT Photometric Hα Survey of the Northern Galactic Plane (IPHAS). This research uses data obtained with the Spitzer Space Telescope. The GMRT is run by the National Centre for Radio Astrophysics of the Tata Institute of Fundamental Research. The National Radio Astronomy Observatory is a facility of the National Science Foundation operated under cooperative agreement by Associated Universities, Inc. This work has been funded by Indo-Thai project, which is supported by Ministry of Higher Education, Science, Research and Innovation (MHESI), Thailand and Department of Science and Technology (DST), India (project No. DST/INT/Thai/P-15/2019). A.Z. thanks the support of the Institut Universitaire de France. D.K.O. acknowledges the support of the Department of Atomic Energy, Government of India (project No. RTI 4002). S.P. acknowledges the DST-INSPIRE fellowship (No. IF180092) of the Department of Science and Technology, India.

Facilities: FCRAO, Gaia, GMRT, Herschel, INT, PANSTARRS1, Spitzer, TNT, UKIRT, VLA.

Software: AIPS (van Moorsel et al. 1996), CASA (McMullin et al. 2007), APLpy (Robitaille & Bressert 2012), Astropy (Astropy Collaboration et al. 2013), CUTEX (Molinari et al. 2011), DS9 (Joye & Mandel 2003; Smithsonian Astrophysical Observatory 2000), IRAF (Tody 1986, 1993), isochrones (Morton 2015), STARLINK (Currie et al. 2014).

ORCID iDs

R. K. Yadav https://orcid.org/0000-0002-6740-7425
M. R. Samal https://orcid.org/0000-0002-9431-6297
E. Semenko https://orcid.org/0000-0002-1912-1342
A. Zavagno https://orcid.org/0000-0001-9509-7316
S. Vaddi https://orcid.org/0000-0003-3295-6595
P. Prajapati https://orcid.org/0000-0002-3094-1077
D. K. Ojha https://orcid.org/0000-0001-9312-3816
J. Jose https://orcid.org/0000-0003-4908-4404
S. Dutta https://orcid.org/0000-0002-2338-4583
P. Irawati https://orcid.org/0000-0002-3348-1491
S. Sharma https://orcid.org/0000-0001-5731-3057
N. Panwar https://orcid.org/0000-0002-0151-2361

References

Alam, S., Albareti, F. D., Allende Prieto, C., et al. 2015, ApJS, 219, 12
Anderson, L. D., Makai, Z., Luisi, M., et al. 2019, ApJ, 882, 11
André, P., Minier, V., Gallais, P., et al. 2008, A&A, 490, L27
André, P., Ward-Thompson, D., & Barsony, M. 2000, in Protostars and Planets IV, ed. V. Mannings, A. P. Boss, & S. S. Russell (Tucson, AZ: Univ. Arizona Press), 59
Ascenso, J., Alves, J., Beletsky, Y., & Lago, M. T. V. T. 2007, A&A, 466, 137
Astropy Collaboration, Robitaille, T. P., Tollerud, E. J., et al. 2013, A&A, 558, A33
Bailer-Jones, C. A. L. 2015, PASP, 127, 994
Bailer-Jones, C. A. L., Rybizki, J., Fouesneau, M., Mantelet, G., & Andrae, R. 2018, AJ, 156, 58
Balser, D. S., Rood, R. T., Bania, T. M., & Anderson, L. D. 2011, ApJ, 738, 27
Banerjee, S., & Kroupa, P. 2015, MNRAS, 447, 728
Banerjee, S., & Kroupa, P. 2017, A&A, 597, A28
Barentsen, G., Farnhill, H. J., Drew, J. E., et al. 2014, MNRAS, 444, 3230
Barentsen, G., Vink, J. S., Drew, J. E., et al. 2011, MNRAS, 415, 103
Battersby, C., Bally, J., Ginsburg, A., et al. 2011, A&A, 535, A128
Beckwith, S. V. W., & Sargent, A. I. 1991, ApJ, 381, 250
Bertoldi, F., & McKee, C. F. 1992, ApJ, 395, 140
Bessell, M. S., & Brett, J. M. 1988, PASP, 100, 1134
Bica, E., Dutra, C. M., & Barbuy, B. 2003, A&A, 397, 177
Binney, J., & Tremaine, S. 2008, Galactic Dynamics (2nd ed.; Princeton, NJ: Princeton Univ. Press)
Bloemen, J. B. G. M. 1987, ApJ, 322, 694
Bodenheimer, P., Tenorio-Tagle, G., & Yorke, H. W. 1979, ApJ, 233, 85
Bonnell, I. A., Vine, S. G., & Bate, M. R. 2004, MNRAS, 349, 735
Bontemps, S., Andre, P., Terebey, S., & Cabrit, S. 1996, A&A, 311, 858
Borissova, J., Pessev, P., Ivanov, V. D., et al. 2003, A&A, 411, 83
Burkert, A., & Hartmann, L. 2004, ApJ, 616, 288
Chambers, K. C., Magnier, E. A., Metcalfe, N., et al. 2016, arXiv:1612.05560
Chen, H.-Y., Chen, X., Wang, J.-Z., Shen, Z.-Q., & Yang, K. 2020, ApJS, 248, 3
Chini, R., & Wink, J. E. 1984, A&A, 139, L5
Comerón, F., & Pasquali, A. 2005, A&A, 430, 541
Currie, M. J., Berry, D. S., Jenness, T., et al. 2014, in ASP Conf. Ser. 485, Astronomical Data Analysis Software and Systems XXIII, ed. N. Manset & P. Forshay (San Francisco, CA: ASP), 391
Damian, B., Jose, J., Samal, M. R., et al. 2021, MNRAS, 504, 2557
Da Rio, N., Robberto, M., Soderblom, D. R., et al. 2010, ApJ, 722, 1092
Das, S. R., Jose, J., Samal, M. R., Zhang, S., & Panwar, N. 2021, MNRAS, 500, 3123
Deharveng, L., Schuller, F., Anderson, L. D., et al. 2010, A&A, 523, A6
Deharveng, L., Zavagno, A., Samal, M. R., et al. 2015, A&A, 582, A1
Dotter, A. 2016, ApJS, 222, 8
Draine, B. T. 2011, Physics of the Interstellar and Intergalactic Medium (Princeton, NJ: Princeton Univ. Press)
Drew, J. E., Greimel, R., Irwin, M. J., et al. 2005, MNRAS, 362, 753
Dunham, M. M., Allen, L. E., Evans, N. J. I., et al. 2015, ApJS, 220, 11
Dutta, S., Mondal, S., Jose, J., et al. 2015, MNRAS, 454, 3597
Dutta, S., Mondal, S., Samal, M. R., & Jose, J. 2018, ApJ, 864, 154
Eden, D. J., Liu, T., Kim, K.-T., et al. 2019, MNRAS, 485, 2895
Elmegreen, B. G., & Lada, C. J. 1977, ApJ, 214, 725
Eswaraiah, C., Li, D., Samal, M. R., et al. 2020, ApJ, 897, 90
Evans, N. J. I., Dunham, M. M., Jørgensen, J. K., et al. 2009, ApJS, 181, 321

Fernández-Martín, A., Pérez-Montero, E., Vílchez, J. M., & Mampaso, A. 2017, A&A, 597, A84
Feroz, F., Hobson, M. P., & Bridges, M. 2009, MNRAS, 398, 1601
Fukuda, N., & Hanawa, T. 2000, ApJ, 533, 911
Gaia Collaboration, Brown, A. G. A., Vallenari, A., et al. 2018, A&A, 616, A1
Gaia Collaboration, Brown, A. G. A., Vallenari, A., et al. 2021, A&A, 650, C3
Gaia Collaboration, Prusti, T., de Bruijne, J. H. J., et al. 2016, A&A, 595, A1
Garay, G., & Lizano, S. 1999, PASP, 111, 1049
Gieles, M. 2010, in IAU Symp. 266, Star Clusters: Basic Galactic Building Blocks Throughout Time and Space, ed. R. de Grijs & J. R. D. Lépine (Cambridge: Cambridge Univ. Press), 69
Gieles, M., & Portegies Zwart, S. F. 2011, MNRAS, 410, L6
Gómez, G. C., & Vázquez-Semadeni, E. 2014, ApJ, 791, 124
Gutermuth, R. A., Megeath, S. T., Myers, P. C., et al. 2009, ApJS, 184, 18
Gutermuth, R. A., Megeath, S. T., Pipher, J. L., et al. 2005, ApJ, 632, 397
Harayama, Y., Eisenhauer, F., & Martins, F. 2008, ApJ, 675, 1319
Hartmann, L., & Burkert, A. 2007, ApJ, 654, 988
Heiter, U., Kupka, F., van't Veer-Menneret, C., et al. 2002, A&A, 392, 619
Heitsch, F., Hartmann, L. W., Slyz, A. D., Devriendt, J. E. G., & Burkert, A. 2008, ApJ, 674, 316
Hillenbrand, L. A. 1997, AJ, 113, 1733
Howard, C., Pudritz, R., & Klessen, R. 2017, ApJ, 834, 40
Hubeny, I., & Lanz, T. 2011, Synspec: General Spectrum Synthesis Program, Astrophysics Source Code Library, ascl:1109.022
Hunter, D. A., & Massey, P. 1990, AJ, 99, 846
Intema, H. T., Jagannathan, P., Mooley, K. P., & Frail, D. A. 2017, A&A, 598, A78
Israel, F. P. 1977, A&A, 60, 233
Jackson, J. M., Rathborne, J. M., Shah, R. Y., et al. 2006, ApJS, 163, 145
Jose, J., Herczeg, G. J., Samal, M. R., Fang, Q., & Panwar, N. 2017, ApJ, 836, 98
Joye, W. A., & Mandel, E. 2003, in ASP Conf. Ser. 295, Astronomical Data Analysis Software and Systems XII, ed. H. E. Payne, R. I. Jedrzejewski, & R. N. Hook (San Francisco, CA: ASP), 489
Kauffmann, J., Pillai, T., & Zhang, Q. 2013, ApJL, 765, L35
Kharchenko, N. V., Piskunov, A. E., Schilbach, E., Röser, S., & Scholz, R. D. 2013, A&A, 558, A53
King, I. 1962, AJ, 67, 471
Kirk, H., Myers, P. C., Bourke, T. L., et al. 2013, ApJ, 766, 115
Kroupa, P. 2001, MNRAS, 322, 231
Kuhn, M. A., Hillenbrand, L. A., Sills, A., Feigelson, E. D., & Getman, K. V. 2019, ApJ, 870, 32
Kumar, M. S. N., Palmeirim, P., Arzoumanian, D., & Inutsuka, S. I. 2020, A&A, 642, A87
Lada, C. J., & Adams, F. C. 1992, ApJ, 393, 278
Lada, C. J., & Lada, E. A. 2003, ARA&A, 41, 57
Lada, C. J., Lombardi, M., & Alves, J. F. 2010, ApJ, 724, 687
Lahulla, J. F. 1985, A&AS, 61, 537
Lanz, T., & Hubeny, I. 2003, ApJS, 146, 417
Lawrence, A., Warren, S. J., Almaini, O., et al. 2007, MNRAS, 379, 1599
Lin, C. C., Mestel, L., & Shu, F. H. 1965, ApJ, 142, 1431
Liu, X.-L., Xu, J.-L., Wang, J.-J., et al. 2021, A&A, 646, A137
Longmore, S. N., Kruijssen, J. M. D., Bastian, N., et al. 2014, in Protostars and Planets VI, ed. H. Beuther et al. (Tucson, AZ: Univ. Arizona Press), 291
Lucas, P. W., Hoare, M. G., Longmore, A., et al. 2008, MNRAS, 391, 136
Mallick, K. K., Kumar, M. S. N., Ojha, D. K., et al. 2013, ApJ, 779, 113
Mallick, K. K., Ojha, D. K., Tamura, M., et al. 2015, MNRAS, 447, 2307
Martins, F., Schaerer, D., & Hillier, D. J. 2005, A&A, 436, 1049
McMullin, J. P., Waters, B., Schiebel, D., Young, W., & Golap, K. 2007, in ASP Conf. Ser. 376, Astronomical Data Analysis Software and Systems XVI, ed. R. A. Shaw, F. Hill, & D. J. Bell (San Francisco, CA: ASP), 127
Mège, P., Russeil, D., Zavagno, A., et al. 2021, A&A, 646, A74
Mezger, P. G., & Henderson, A. P. 1967, ApJ, 147, 471
Minniti, D., Lucas, P. W., Emerson, J. P., et al. 2010, NewA, 15, 433
Molinari, S., Schisano, E., Faustini, F., et al. 2011, A&A, 530, A133
Molinari, S., Swinyard, B., Bally, J., et al. 2010, A&A, 518, L100
Morton, T. D. 2015, isochrones: Stellar Model Grid Package, Astrophysics Source Code Library, ascl:1503.010
Motte, F., Bontemps, S., & Louvet, F. 2018, ARA&A, 56, 41
Murray, N. 2009, ApJ, 691, 946
Myers, P. C. 2009, ApJ, 700, 1609
Naranjo-Romero, R., Vázquez-Semadeni, E., & Loughnane, R. M. 2020, arXiv:2012.12819
Neichel, B., Samal, M. R., Plana, H., et al. 2015, A&A, 576, A110
Oey, M. S., & Kennicutt, R. C. J. 1997, MNRAS, 291, 827
Panwar, N., Pandey, A. K., Samal, M. R., et al. 2018, AJ, 155, 44
Panwar, N., Samal, M. R., Pandey, A. K., Singh, H. P., & Sharma, S. 2019, AJ, 157, 112
Patten, B. M., Stauffer, J. R., Burrows, A., et al. 2006, ApJ, 651, 502
Pecaut, M. J., & Mamajek, E. E. 2013, ApJS, 208, 9
Pellegrini, E. W., Oey, M. S., Winkler, P. F., et al. 2012, ApJ, 755, 40
Peretto, N., Fuller, G. A., André, P., et al. 2014, A&A, 561, A83
Pfalzner, S., & Kaczmarek, T. 2013, A&A, 559, A38
Pfalzner, S., Kirk, H., Sills, A., et al. 2016, A&A, 586, A68
Pilbratt, G. L., Riedinger, J. R., Passvogel, T., et al. 2010, A&A, 518, L1
Pon, A., Johnstone, D., & Heitsch, F. 2011, ApJ, 740, 88
Preibisch, T., & Mamajek, E. 2008, in Handbook of Star Forming Regions, Volume II: The Southern Sky, ed. B. Reipurth (San Francisco, CA: ASP), 235
Rieke, G. H., & Lebofsky, M. J. 1985, ApJ, 288, 618
Robitaille, T., & Bressert, E. 2012, APLpy: Astronomical Plotting Library in Python, Astrophysics Source Code Library, ascl:1208.017
Rubin, R. H. 1968, ApJ, 154, 391
Ryabukhina, O. L., Zinchenko, I. I., Samal, M. R., et al. 2018, RAA, 18, 095
Salpeter, E. E. 1955, ApJ, 121, 161
Samal, M. R., Deharveng, L., Zavagno, A., et al. 2018, A&A, 617, A67
Samal, M. R., Ojha, D. K., Jose, J., et al. 2015, A&A, 581, A5
Samal, M. R., Pandey, A. K., Ojha, D. K., et al. 2007, ApJ, 671, 555
Samal, M. R., Pandey, A. K., Ojha, D. K., et al. 2010, ApJ, 714, 1015
Schneider, N., Csengeri, T., Hennemann, M., et al. 2012, A&A, 540, L11
Sharpless, S. 1959, ApJS, 4, 257
Sills, A., Rieder, S., Scora, J., McCloskey, J., & Jaffa, S. 2018, MNRAS, 477, 1903
Smith, N., Povich, M. S., Whitney, B. A., et al. 2010, MNRAS, 406, 952
Smithsonian Astrophysical Observatory 2000, SAOImage DS9: A Utility for Displaying Astronomical Images in the X11 Window Environment, Astrophysics Source Code Library, ascl:0003.002
Sokolov, V., Wang, K., Pineda, J. E., et al. 2017, A&A, 606, A133
Swarup, G., Ananthakrishnan, S., Kapahi, V. K., et al. 1991, CSci, 60, 95
Tenorio-Tagle, G. 1979, A&A, 71, 59
Tody, D. 1986, Proc. SPIE, 627, 733
Tody, D. 1993, in ASP Conf. Ser. 52, Astronomical Data Analysis Software and Systems II, ed. R. J. Hanisch, R. J. V. Brissenden, & J. Barnes (San Francisco, CA: ASP), 173
van Moorsel, G., Kemball, A., & Greisen, E. 1996, in ASP Conf. Ser. 101, Astronomical Data Analysis Software and Systems V, ed. G. H. Jacoby & J. Barnes (San Francisco, CA: ASP), 37
Vázquez-Semadeni, E., Palau, A., Ballesteros-Paredes, J., Gómez, G. C., & Zamora-Avilés, M. 2019, MNRAS, 490, 3061
Verschuur, G. L., & Kellermann, K. I. 1988, Galactic and Extra-galactic Radio Astronomy (Berlin: Springer)
Walborn, N. R., & Fitzpatrick, E. L. 1990, PASP, 102, 379
Walch, S., Whitworth, A. P., Bisbas, T. G., Hubber, D. A., & Wünsch, R. 2015, MNRAS, 452, 2794
Weidner, C., Kroupa, P., & Bonnell, I. A. D. 2010, MNRAS, 401, 275
Weidner, C., Kroupa, P., Nürnberger, D. E. A., & Sterzik, M. F. 2007, MNRAS, 376, 1879
Whitney, B. & GLIMPSE360 Team 2009, BAAS, 41, 715
Williams, J. P., & Cieza, L. A. 2011, ARA&A, 49, 67
Wright, E. L., Eisenhardt, P. R. M., Mainzer, A. K., et al. 2010, AJ, 140, 1868
Yadav, R. K., Pandey, A. K., Sharma, S., et al. 2016, MNRAS, 461, 2502
Yorke, H. W., Bodenheimer, P., & Tenorio-Tagle, G. 1982, A&A, 108, 25
Yu, P.-C., Yu, C.-H., Lee, C.-D., et al. 2018, AJ, 155, 91
Yuan, L., Li, G.-X., Zhu, M., et al. 2020, A&A, 637, A67